Signatures of Dipolarizing Flux Bundles in the Nightside Auroral Zone

Mark J. Engebretson[1], Sean A. Gaffaney[1], Jesus A. Ochoa[1], Andrei Runov[2], James M. Weygand[2], Yukitoshi Nishimura[3], Michael D. Hartinger[4, 2], Vyacheslav A. Pilipenko[5], Mark B. Moldwin[6], Martin G. Connors[7], Ian R. Mann[8], Zhonghua Xu[9], and Juan V. Rodriguez[10,11]

(1) Augsburg University
(2) EPSS UCLA
(3) Boston University
(4) Space Science Institute, Boulder
(5) Space Research Institute, Moscow
(6) University of Michigan
(7) Athabasca University
(8) University of Alberta
(9) Virginia Tech
(10) Cooperative Institute for Research in Environmental Sciences, University of Colorado Boulder
(11) NOAA National Centers for Environmental Information

submitted to the Journal of Geophysical Research: Space Physics
November 7, 2023

Key Words: Dipolarizing flux bundles (DFBs), Bursty bulk flows (BBFs), geomagnetic disturbances (GMDs), nighttime magnetic perturbation events (MPEs), auroral images

Key Points:

Geomagnetic disturbances observed in ground magnetometer data can coincide with dipolarizing flux bundles observed by THEMIS spacecraft.

Auroral imager and spherical elementary currents systems maps show excitation of localized upward currents and auroras during these events.

Coincident isolated GMDs and DFBs are strongly associated with high solar wind velocity but not with geomagnetic storms.

Abstract

Dipolarizing flux bundles (DFBs) have been suggested to transport energy and momentum from regions of reconnection in the magnetotail to the high latitude ionosphere, where they can generate localized ionospheric currents that can produce large nighttime geomagnetic disturbances (GMDs). In this study we identified DFBs observed in the midnight sector from ~7 to ~10 R_E by THEMIS A, D, and E during days in 2015-2017 whose northern hemisphere magnetic footpoints mapped to regions near Hudson Bay, Canada, and have compared them to GMDs observed by ground magnetometers. We found six days during which one or more of these DFBs coincided to within ± 3 min with ≥ 6 nT/s GMDs observed by latitudinally closely spaced ground-based magnetometers located near those footpoints. Spherical elementary current systems (SECS) maps and all-sky imager data provided further characterization of two events, showing short-lived localized intense upward currents, auroral intensifications and/or streamers, and vortical perturbations of a westward electrojet. On all but one of these days the coincident DFB – GMD pairs occurred during intervals of high-speed solar wind streams but low values of SYM/H. In some events, in which the DFBs were observed closer to Earth and with lower Earthward velocities, the GMDs occurred slightly earlier than the DFBs, suggesting that braking had begun before the time of the DFB observation. This study is

the first to connect spacecraft observations of DFBs in the magnetotail to intense (>6 nT/s) GMDs on the ground, and the results suggest DFBs could be an important driver of GICs.

1. Introduction

Dipolarizing flux bundles (DFBs) are defined observationally as transient (~ 1 min) magnetotail flux tubes (usually with diameters < ~3 R_E in XGSM and YGSM coordinates) with a significantly more dipolar (northward) magnetic field than their background and a with a density lower than the surrounding plasma. They typically propagate Earthward at high speed, ~ 300 km/s, but in individual events up to 500-800 km/s (Runov et al., 2009, 2011) from a reconnection site deeper in the magnetotail (Liu et al, 2013a, 2014) and eventually stop near the inner edge of the plasma sheet (Liu et al., 2017). They are enveloped in larger 10 min time scale Earthward-moving bursty bulk flows (BBFs, as originally identified by Angelopoulos et al. (1992, 1994). Dipolarization fronts, ion gyro-scale boundaries separating the plasma inside DFB from the ambient plasma sheet and characterized by a small amplitude negative Bz variation followed by a sharp increase in Bz of ~tens of nT, are often observed at the leading edge of BBFs (Runov et al., 2012, Ohtani et al., 2004). The time that such an increase in Bz is observed is used as the time of the DFB (Liu et al., 2013a).

Both the ion pressure and bulk velocity are observed to increase about 1 min before dipolarization front crossings (e.g., Figures 5 and 6 of Runov et al., 2011). Zhou et al. (2010, 2011) noted that an earthward streaming ion population increased as the dipolarization front moved nearer to Earth, and test particle simulations showed that this observed ion distribution was consistent with a picture of ions reflected and accelerated by the approaching front, and suggested that the incoming front could be decelerated by these reflected ions. Li et al. (2011) suggested a complementary picture in that a pressure gradient ahead of the front could be built up by the streaming population, which might result in acceleration of the ambient plasma without direct interaction with the dipolarization front.

The impact of DFBs on the ionosphere was outlined in an event study by Runov et al. (2011). A DFB impacting the near-Earth transition region led to the formation of a system of field-aligned currents that reached the ionosphere (e.g., Sergeev et al., 2014, Birn et al., 2019). FAC closure through intensified westward electrojet currents resulted in perturbations in the geomagnetic field observed by ground-based magnetometers (McPherron et al., 1973) and the formation of a north-south auroral form, as reported also in earlier studies (Sergeev et al., 2000a, 2000b; Nakamura et al., 2001) and documented in recent reviews (Forsyth et al., 2020; Lyons et al., 2022).

Much of the focus on BBFs and DFBs has been on the impact of a series of these events during or preceding substorms (e.g., Liu et al., 2013a). Much less attention has been paid to the presence and impact of isolated BBF / DFB events, which have been suggested as possible drivers of large, isolated nighttime geomagnetic disturbances (GMDs), also known as magnetic perturbation events (MPEs).

What is new about this current study is its focus on large, isolated geomagnetic disturbances (GMDs) at auroral zone latitudes that often have amplitudes > 6 nT/s (> 360 nT/min), and thus are capable of exciting geomagnetically induced currents (GICs) in susceptible infrastructure (Engebretson et al., 2019a,b; 2021a,b, Weygand et al., 2021). The introduction of Zou et al. (2022) provides a review of the several varieties of auroras that are associated with large dB/dt events, including spatially localized ones. Engebretson et al. (2019b) and Weygand et al. (2021) showed examples of localized GMDs that were accompanied by localized equivalent ionospheric currents, localized pairs of upward/downward vertical currents (proxies for field-aligned currents), and poleward boundary intensifications and/or auroral streamers. Engebretson et al., (2019a,b) found that the horizontal half-amplitude radius of these GMDs was ~275 km, and Weygand et al. (2021) reported a range of ~250-450 km for several events, with a somewhat greater longitudinal extent in some cases.

Section 2 describes the data set of DFBs and the ground magnetometers with whose data they are compared. Section 3 presents detailed case studies of intervals on two days that also include all-sky auroral imager data and maps of equivalent ionospheric and vertical currents over North America produced using the spherical elementary currents (SECS) method. Section 4 provides detailed timing and geophysical context information for DFB-GMD events during six days that occurred within ± 3 min of each other. Composite figures showing the time series of the DFBs and GMDs during the other four days are provided in the Supporting Information. Section 5 discusses some of the challenges in identifying these events and the implications of their relative timing, and section 6 summarizes our findings.

2. Instrumentation and Data Set

The Time History of Events and Macroscale Interactions during Substorms (THEMIS) set of five-spacecraft were launched in 2007 into highly elliptical orbits with apogees of 10, 12, 12, 20, and 30 R_E. (Angelopoulos, 2008; Sibeck and Angelopoulos, 2008). In 2010 the two spacecraft with the highest apogee were moved into lunar orbit and comprise the Acceleration, Reconnection, Turbulence and Electrodynamics of Moon's Interaction with the Sun (ARTEMIS) mission, and the apogees of the other three spacecraft have been fixed at ~12 R_E in orbits separated by approximately 500 to 3000 km

The Fluxgate Magnetometer (FGM) instrument on the THEMIS spacecraft (Auster et al., 2008) provides DC magnetic field measurements with a temporal resolution of 128 vectors per second during the burst mode. The Electrostatic Analyzer (ESA) (McFadden et al., 2008) provides ion and electron distribution functions in the 5 eV to 25 keV energy range with a time resolution of one 3-D distribution function per spin in the burst mode. The Solid State Telescope (SST) (Angelopoulos, 2008) detects high-energy (30 keV - 1 MeV) ion and electron fluxes with a time resolution of one 3-D distribution function per spin in the burst and reduced modes.

The Magnetospheric Electron Detector (MAGED) and Magnetospheric Proton Detector (MAGPD) on GOES 13-15 in geostationary orbit measure 30-600 keV electron fluxes and 80-800 keV proton fluxes, respectively, in five energy bands (Hanser, 2011). Each instrument consists of nine identical-design telescopes in a cruciform arrangement (Sillanpää et al., 2017). Co-manifested with MAGED and MAGPD are a pair of fluxgate magnetometers (inboard and outboard) on a boom (Califf et al., 2023). Pitch angles for MAGED and MAGPD are calculated from the magnetic field vectors by the outboard magnetometer.

Ground-based magnetometer data used in this study were recorded by stations in the MACCS (Engebretson et al., 1995), AUTUMNX (Connors et al., 2016), CARISMA (Mann et al., 2008), and CANMOS (Nikitina et al., 2016), arrays in Arctic Canada, as detailed in Table 1 and Figure 1 (red circles). Figure 1 shows the locations of the magnetometers in the Hudson Bay region that have been used in this study, as well as the northern hemisphere magnetic field footpoints of geosynchronous spacecraft GOES 13 and 14. Table 1 lists the locations of these magnetometers in geographic and geomagnetic coordinates, and Table 2 lists the geographic distances between the stations located in two latitudinal chains along the west and east coasts of Hudson Bay, respectively. The sampling cadence of these instruments, 1.0 or 0.5 s, permits viewing the full detail of the GMDs reported here, including their derivative amplitudes (e.g., the several examples comparing time series with these cadences to down-sampled 1-min data shown by Zou et al., 2022).

This study also makes use of all-sky white-light images produced by THEMIS imagers (Mende et al. 2008, Donovan et al. 2006), the Redline Emission Geospace Observatory (REGO) 630.0 nm all-sky images, and maps of equivalent ionospheric and vertical currents (a proxy for field-aligned currents) over North America produced using the Spherical Elementary Current Systems (SECS) technique (Amm and Viljanen, 1999, Weygand et al., 2009a, b, 2011).

Our study focuses on DFBs observed by THEMIS A, D, and E during 2015, 2016, and 2017, the three years during the solar cycle that coincided with the largest number of ≥ 6 nT/s GMDs identified during solar cycle 24 in observations by several MACCS magnetometers in eastern Arctic Canada (Engebretson et al., 2023). Candidate events on 198 days satisfied two initial criteria: they were observed during passes over the North American continent, and their ~12 R_E apogees were within ~3 h MLT of local midnight. The NASA SSCWEB utility was then used to display approximate mappings of the northern hemisphere footpoints of the magnetic field line through the relevant THEMIS spacecraft of candidate events in order to identify events that mapped to the region from west of Hudson Bay to east of Hudson Bay shown in Figure 1. Each event during the resulting 48 days was compared to ground magnetometer data from the stations near the east and west coasts of Hudson Bay shown in Figure 1. Events during which the DFBs mapped to the center of Hudson Bay typically produced little or weak GMD activity at the magnetometer sites on either the west or east coast, and were excluded from further consideration. Events with temporally overlapping DFBs were also excluded regardless of the presence of large GMDs. However, during six of these days one or more clear and isolated DFBs occurred within ± 3 min of GMDs at one or more of these stations.

3. Example Events

Two events will be presented in detail in this section; on both days all-sky auroral images were available before, during, and after nearly simultaneous DFBs and GMDs.

3.1 January 27, 2017

On this day two GMDs occurred within ~15 minutes of each other while THEMIS D and THEMIS-E were nearly overhead of the FCHU-BACK-GILL chain of magnetometers near the southwestern edge of Hudson Bay. The Fort Smith imager's range extended over these three stations but did not reach to Rankin Inlet.

Figure 2 shows IMF and solar wind data from OMNI data base, time-shifted to the nose of the bow shock, as well as three magnetic activity indices (AL, AU, and SYM/H) from 05:20 to 06:20 UT on this day. The two shaded regions indicate time intervals with nearly simultaneous DFBs observed by THEMIS D and GMDs observed by the ground magnetometers located along the west coast of Hudson Bay. Each region is also highlighted in Figure 4 and will be examined in greater detail in Figures 5 and 6. During the period shown and during both shaded intervals the IMF Bx component was negative and the By component was positive. The Bz component was mostly near 0 nT before the first shaded interval, rose to ~7 nT near 05:45 UT and remained positive until 05:59 UT, neared 0 nT twice during the second interval before becoming slightly negative near 06:06 UT, and became positive again at 06:09 UT. The solar wind velocity (Vsw) exceeded 565 km/s throughout the period shown. It rose to 630 km/s between 05:42 and 05:45 UT, one min after the start of the first shaded interval and just before a data gap. Data resumed at 05:50 UT, at which time Vsw was at 580 km/s. During the second shaded interval Vsw was again near 640 km/s. Before and during the two shaded intervals the solar wind proton number density (Nsw) varied between 4 and 8 cm^{-3} and the solar wind dynamic pressure (Psw) varied similarly between 4 and 8 nPa.

The AL index decreased from -100 nT at 05:20 UT to -300 nT at 05:44, the beginning of the first shaded interval, and dropped more rapidly to -600 nT by 05:49. AL increased slightly during the middle of the second interval to -400 nT, and subsequently decreased to ~-750 nT. The AU index ranged between 50 and 250 nT during the period shown, with values near 150 nT during both intervals. The SYM/H index varied only slightly throughout the period shown, from -10 to -18 nT, indicating little geomagnetic storm activity. The Newell and Gjerloev (2011), Forsyth et al. (2015), and Ohtani and Gjerloev (2020) substorm lists (each accessed on the SuperMAG web site at https://supermag.jhuapl.edu/substorms/) all included a substorm onset near 05:22 UT, but onsets at 05:44 UT and 06:04 UT were included only in the Newell and Gjerloev (2011) list. The combination of high Vsw, -10 to -20 nT SYM/H, and moderate auroral activity (AL and AU) including substorm activations is characteristic of a High Intensity Long

Duration Continuous AE Activity (HILDCAA) interval, as described by Tsurutani and Gonzalez (1987). Tsurutani et al. (1995) noted that similar extended HILDCAA intervals observed during the declining phase of the sunspot cycle were characterized by continuous auroral substorms stimulated by large-amplitude Alfvén waves within the high-speed streams.

Figure 3 shows a summary plot of THEMIS D observations between 05:20 and 06:20 UT on January 27, 2017. Shown are magnetic field components (panel a), electron and ion time-energy spectrograms (panels b and c), ion density (panel d), ion and electron temperatures (panel 3), and ion bulk velocity (panel f). It is evident from these observations that prior to the plasma sheet expansion at 05:45 UT, associated with a decrease in the magnetic field strength, the density and temperature increased, and with enhancement in the ion bulk flow, THEMIS D was at the plasma sheet boundary layer south of the neutral sheet (as evidenced by the negativemagnetic field component Bx). Weak signatures of DFBs were observed shortly thereafter, at 05:46:58 and 05:48:20 UT. Notably, the Bx magnitude reached 70.5 nT and then dropped to 30 nT during the plasma expansion. It is also worthy of note that although energies of both ions and electrons increased during the plasma sheet expansion, the increase in the electron energy was larger than that of the ions. Immediately after the expansion associated with a distinct magnetic field structure, characterized by a Bz jump, sharp By rotation, and drop in |Bx|, THEMIS D started to detect a significant flux of electrons at the energy of 100 keV. Correspondingly, the electron temperature increased during the expansion from ~100 eV to ~5 keV and became comparable with the ion temperature.

A later, more distinct DFB was detected by THEMIS D at 05:59 UT. It was associated with a drop in the density and an enhancement in the ion bulk velocity. THEMIS D also detected electron injections at energies exceeding 100 keV. The electron temperature increased again up to ~5 keV and became close to the ion temperature.

Figure 4 shows simultaneous observations from THEMIS-D and four ground-based magnetometers along the west coast of Hudson Bay, in order of decreasing latitude, from 05:20 to 06:20 UT January 27, 2017. Panels a and b show the GSM vector components of the magnetic field and bulk velocity observed by THEMIS-D (repeated from Figure 3). DFBs were identified at 05:46:58, 05:48:20, and 05:59:23 UT. Panels c, d, e, and f show three components of the time derivative of the magnetic field from Rankin Inlet, Fort Churchill, Back, and Gillam, respectively, in local geomagnetic coordinates. The derivative amplitude of the first large GMD, observed between 05:44 and 05:53 UT, was largest at Fort Churchill at 05:48 UT in the By component (9.38 nT/s) and Bz component (-9.11 nT/s), successively weaker to the south at Back Lake and Gillam, and much weaker to the north at Rankin Inlet. The derivative amplitude of the second large GMD, observed between 5:58 and 06:09 UT, was largest at Rankin Inlet at 06:01 UT in the Bx component (-12.08 nT/s) and at 06:03 UT in the By component (9.65 nT/s), but also reached peak values above 6 nT/s at each of the three other stations. The relative timing of the DFBs and GMDs will be discussed in section 4 below.

Figure 5 shows composite all-sky images and SECS maps at 05:44, 05:47:30, and 05:53 UT January 27, 2017, before, during, and after the first DFB-GMD pair shown in Figure 4.

Panels a, b, and c of Figure 5 are images from a movie (included in the Supporting Information) prepared by the THEMIS project showing all sky camera mosaics from Fort Smith and The Pas projected geographically onto a map of central and eastern Canada. The fields of view of the cameras are evident from the two circles. Parallels and meridians in magnetic coordinates are shown in white, and the light blue meridian denotes local magnetic midnight. The pink, aqua, and blue squares denote the footpoints of THEMIS-A, -D, and -E, respectively, determined using the Tsyganenko-2001 magnetic field model (Tsyganenko, 2002a,b) for field line tracing. The locations of Rankin Inlet, Fort Churchill, Back Lake, and Gillam near the western edge of Hudson Bay are shown by red crosses. Rankin Inlet was located beyond the range of the imager. The yellow dot shows the magnetic footpoint of GOES 14.

The footpoints of the three THEMIS spacecraft were nearly stationary in panels a, b, and c of Figure 5, with THEMIS A slightly northwest of Fort Churchill, THEMIS D just east of Back Lake, and THEMIS E slightly farther to the northeast, over southwestern Hudson Bay. Only very weak auroras appeared anywhere in the field of view of the imagers at 05:44 UT (panel a), before the start of the first GMD shown in Figure 4. At 05:47:30 UT (panel b), near the time of the largest derivative of the GMD in the FCHU data, bright east-west arcs appeared far to the west of Hudson Bay and the tip of an arc appeared over Fort Churchill, partly obscured by the pink square. At 05:53 UT (panel c), at the end of the GMD, the sky was dark over and near Fort Churchill, but complex auroral arcs filled much of the region to the west. An auroral streamer (N-S arc) was found just to the west of the THEMIS-A footpoint and on the GOES 14 footpoint. The weak auroral glow that appeared over and to the south of Gillam at 5:44 was unchanged by 05:47:30; it became weaker at Gillam by 5:53 UT but brightened slightly to the south.

Panels d, e, and f of Figure 5 are SECS maps of the equivalent ionospheric currents (black arrows) and vertical current intensities (upward in red, downward in blue) across northern North America and western Greenland. The stars show the locations of magnetometers providing data on this day, and the dots show grid points at which the currents were calculated. The yellow circle in each of these maps outlines the region of interest; the four stars it encloses correspond to the locations of the magnetometer stations near the western edge of Hudson Bay.

Panel d of Figure 5 shows that at 05:44 UT a narrow westward electrojet passed through Back Lake, and a weak downward current region (blue) extended westward of Back Lake and Fort Churchill. At 5:47:30 an intense, localized upward current (red) appeared above Back Lake and Fort Churchill, and the westward electrojet above these and nearby stations developed a counterclockwise rotation. At 5:53 UT a more strictly westward electrojet reappeared over these stations, the region of downward current expanded southward to Back Lake, and only a weak upward current remained, at this time over Gillam.

Figure 6 shows composite all-sky images and SECS maps at 05:58:30, 06:01:30, and 06:09 UT on January 27, 2017, before, during and after the second DFB-GMD pair shown in Figure 4. The footpoints of the three THEMIS spacecraft resumed their slow westward motion during this time interval, with THEMIS A slightly northwest of Fort Churchill, THEMIS D above and later slightly west of Back Lake, and THEMIS E approaching the southwestern coast of Hudson Bay. Weak auroras appeared at some distance to the south and west of Hudson Bay at 05:58:30 UT (panel a), before the start of the second GMD shown in Figure 4, but there was very little auroral intensity above any of the magnetometer stations. At 06:01:30 UT (panel b), shortly after the time of the largest derivative in the Back Lake data, bright and narrow auroral streamers appeared to the west of Fort Churchill and Back Lake, and a wider streamer appeared to the northeast and immediately southwest of Gillam. By 06:09 UT (panel c), several minutes after the end of the intense GMD, the streamers became faint and moved to the footpoint of GOES 14. Only weak auroral activity remained over these three magnetometer stations.

Panel d of Figure 6 shows that at 05:58:30 UT a narrow westward electrojet passed through Back Lake before turning to the northwest, and a weak downward current region (blue) extended westward of Back Lake and Fort Churchill. At 6:01:30 UT (panel e) a moderately strong localized upward current (red) appeared between Rankin Inlet and Fort Churchill, and the westward electrojet veered to the northwest in a partial counterclockwise vortex and resumed its westward orientation north of Rankin Inlet in association with a downward current. This structure in the currents, similar to that noted in panel e of Figure 5, is most likely consistent with the streamer wedge current system shown in the schematic diagram of auroral streamers and associated currents in Figure 1 of Weygand et al. (2022). At 6:09 UT (panel f) a more consistently westward electrojet reappeared over these stations, the region of upward current moved southward to between Back Lake and Gillam, and only weak downward current remained near Fort Churchill.

As is indicated in Figures 1, 5, and 6, the footpoint of GOES 14 (determined using SSCWEB) was located ~590 km southwest of Fort Churchill, and west of the streamers overhead of the magnetometer stations. Figure 7 shows stacked plots of the differential electron flux (panel a) and ion flux (panel b) recorded by telescope 1, the Hp component of the magnetic field observed by GOES 14 (panel c), and the SMU (red) and SML (blue) indices (panel d), from 05:20 to 06:20 UT. The fluxes shown in Figures 7a and 7b were observed by Telescope 9 of GOES-14 MAGED and MAGPD. Because GOES-14 was flying inverted during this period, Telescope 9 of each instrument was looking southward in the anti-field-aligned direction, thus observing the most nearly field-aligned fluxes (Jaynes et al. 2013). The pitch angles vary with the natural variations in the geomagnetic field orientation observed by the GOES-14 magnetometer (Rodriguez, 2014). During 0520-0620, the Telescope 9 central pitch angle was on average 12.4 deg with a range of 5.7 to 23.5 deg. The bounce loss cone in GEO (~2.5 deg) is much smaller than the MAGED and MAGPD telescope FOV (20 deg FWHM). Owing to the satellite orientation, the FOV size and the small central pitch angles, the Telescope 9 FOV fluxes included both loss-cone and near-loss-cone fluxes during most of this period, as in the case studied by Jaynes et al. (2013)."

Electron fluxes (Figure 7a) showed sharp increases at 05:51 and 06:05, in each case shortly after the maxima in the GMDs shown in Figure 4, and flux peaks at ~05:54 and ~05:06 UT. Smaller increases in ion flux (Figure 7b) appeared slightly earlier, at 05:49 and 06:01 UT, and increases in Hp, indicating dipolarizations occurred near 05:54 and 06:04 UT (Figure 7c). The large downward trend in SML from 05:20 to 06:20 UT (Figure 7d) is indicative of increasing substorm activity.

Movie S1 shows the progression of auroral streamers from 05:30 to 06:11 UT on January 27, 2017. During the first DFB-GMD interval there was only very weak auroral activity above the GOES 14 footpoint (shown in Figures 5 and 6 but not in the movie) before 05:50 UT; a complex streamer heading southeast appeared near 05:51 UT, was strongest near that footpoint at 05:54 UT, and then faded away. During the second interval the narrow streamer west of and clearly separated from the V-shaped streamer observed near the magnetometer stations at 06:01:30 moved westward and both broadened and intensified under the G14 footpoint at 06:05 UT. It then remained relatively stationary until 06:09 UT, and by 06:11 UT it had moved farther westward and weakened. The timing of the changes shown in these ASI images is consistent with the increases in electron fluxes shown in Figure 7a. The lack of simultaneity between the electron flux peaks observed by GOES and the DFBs and GMDs, suggesting they are due to independent processes, is consistent with the ~450 km longitudinal separation between the GOES 14 magnetic footpoint and the magnetometer stations and the highly localized nature of the GMDs and their associated field-aligned currents and auroral signatures.

3.2 January 7, 2017

On this day four DFBs appeared at THEMIS E within a span of 80 min. Nearly simultaneous GMDs coincided with the first three of them at Salluit and more weakly at Puvurnituq near the northeast corner of Hudson Bay, and the first and third coincided with GMDs at Cape Dorset, on the southwest coast of Baffin Island. The all-sky imager at Rankin Inlet extended eastward nearly to these stations.

No time-shifted OMNI data were available during this interval. Although IMF and solar wind date were available near the L1 point from ACE, DSCOVR, and WIND, their values showed moderate to large disagreements in all three magnetic field components, as well as in Nsw, Psw, and Vsw. We show instead in Figure 8 time-corrected IMF and solar wind data from ARTEMIS P2 (THEMIS C), in orbit around the moon at X_{GSM} = -16.70 R_E, Y_{GSM} = 52.33 R_E, Z_{GSM} = 1.26 R_E, ~5 min downstream of Earth's bow shock and azimuthally at a similar distance from the Earth-Sun line as WIND. The shaded region in Figures 8 and 9 indicates a time interval to be examined in greater detail in Figure 11.

Figures 8a and b show that the IMF Bx component varied in direction often during this 80 min interval, while IMF By varied with similar amplitude but was mostly negative. IMF Bz (Figure 8d) was negative and nearly steady before and during the first DFB – GMD event shown in Figures 9 and 10 at 4:50 UT, was positive before returning to -3 nT shortly before the second and third DFB – GMD events at 05:10 and 05:20 UT, and was again steadily negative during the fourth DFB – GMD event at 05:50 UT. The earthward component of Vsw, the solar wind speed (Figure 8d), was near 700 km/s until ~05:20 UT, when it dropped briefly to 625 km/s, but then gradually increased to ~680 km near the end of the interval. Vsw was high before this interval as well: during all of the previous day (January 6) and up to the OMNI data gap near 04:30 UT on January 7, OMNI data (not shown) indicated that Vsw exceeded 650 km/s. Figure 8e shows that the solar wind density Nsw was at or below 3 cm^{-3} throughout this interval. The solar wind dynamic pressure Psw, shown in Figure 8f, remained below 3 nPa throughout this interval; its variations were very similar to those of Nsw. The AL index (Figure 8g) varied between -20 and -125 nT during the 80 min, but was steady near -80 nT during the third DFB – GMD event (the shaded interval). The AU index (Figure 8h) varied between 50 and 200 nT, and was also steady (near 100 nT) during the shaded interval. The SYM/H index (Figure 8i) varied only slightly throughout the period shown, from -12 to -16 nT, again indicating little geomagnetic storm activity.

The Newell and Gjerloev (2011) and Forsyth et al. (2015) substorm lists on SuperMAG included a substorm onset near 05:23 UT, and an onset at 04:48 UT was included only in the Forsyth et al (2015) list. Both of these onsets occurred slightly before GMDs appeared at THEMIS E. This interval is again typical of HILDCAA events.

Figure 9 shows a summary plot of THEMIS E observations between 04:40 and 06:00 UT on January 7, 2017 in the same format as in Figure 3. Evidently, the probe was deep in the plasma sheet near the magnetic equator. The plasma sheet was abundant with energetic electrons: significant fluxes of electrons were detected at energies of 100 to 500 keV. During the interval of interest, THEMIS detected a set of quasi-recurrent magnetic field dipolarizations (increases in Bz) at 04:51:27, 05:09:20, and 05:25:12 UT. The dipolarizations were preceded by intervals of magnetic field stretching, characterized by increases in Bx magnitude and decreases in Bz. Each dipolarization was associated with a decrease in density, which is characteristic of DFBs, an enhancement in the plasma bulk flow, and an energetic (up to 700 keV) electron injection. No significant energetic ion injections were detected. The electron temperature increased at each dipolarization and became comparable and even exceeded the ion temperature. It is also worth noticing that the bulk flow enhancements exhibited vorticity: large-amplitude variations with sign changes were detected in all three velocity components. The evident flow vorticity might indicate that the bursty flows associated with the dipolarizations were detected at or close to their stoppage points (e.g., Panov et al., 2010, 2013, Birn et al., 2019).

Figure 10 shows simultaneous observations from THEMIS E and five ground-based magnetometers near the east coast of Hudson Bay, in order of decreasing latitude, from 04:40 to 06:00 UT January 7, 2017, as in Figure 5. Panels a and b show the GSM vector components of the magnetic field and bulk velocity observed by THEMIS E (repeated from Figure 9). DFBs were identified at 04:51:27, 05:09:20, and 05:25:12 UT. Panels c, d, e, and f show three components of the time derivative of the magnetic field from Cape Dorset, Salluit, Puvurnituq, Inukjuak, and Kuujuarapik, respectively, in local geomagnetic coordinates. Amplitudes of the GMDs at times corresponding to all three DFBs exceeded 6 nT/s at Salluit; the largest dB/dt value was 9.50 nT/s in the Bz component at 05:27 UT The relative timing of all three DFB – GMD pairs will be discussed in section 4 below.

Figure 11 shows all-sky images and SECS maps at 05:19, 05:26, and 05:32 UT on January 7 2017, before, during and after the DFB-GMD pair shown in Figure 9.

Panels a, b, and c of Figure 11 are images from a movie (included in the Supporting Information) prepared by the REGO project showing all sky camera views from Rankin Inlet projected geographically onto a map of the Hudson Bay region. The images are dominated by bright light from the moon (left) and the town (below), but these do not obscure the region of interest, located at the eastern edge of the image. The locations of Cape Dorset, Salluit, Puvurnikuq, Inukjuaq, and Kuujuarapik near the eastern edge of Hudson Bay are shown by red crosses. The aqua and purple boxes at the right show the magnetic footpoints of THEMIS D and E, mapped using the Tsyganenko-2001 (T01) magnetic field model. THEMIS D mapped to a location slightly west of Inukjuaq, and THEMIS E mapped to a location slightly east of Puvurnituq.

Only very weak and featureless auroras appeared near the four northern stations at 05:19 UT (panel a), before the start of the GMD shown in Figure 10. At 05:26 UT (panel b), shortly before the time of the largest derivatives in the Cape Dorset and Salluit data, moderately bright east-west arcs appeared at the eastern edge of the field of view near those stations. At 05:32 UT (panel c), at the end of the GMD, relatively weak aurora was again featureless near the four northern stations, but moderately bright and complex auroral arcs filled much of the region above the western half of Hudson Bay.

Panels d, e, and f of Figure 11 are SECS maps of the equivalent ionospheric currents (black arrows) and vertical current intensities (upward in red, downward in blue) across northern North America. The stars show the locations of magnetometers providing data on this day, and the dots show grid points at which the currents were calculated. The yellow circle in each of these maps outlines the region of interest; the four stars it encloses correspond to the locations of the magnetometer stations.

As in Figure 5, the yellow circles in the SECS maps in panels d, e, and f of Figure 11 enclose a region that includes the ground magnetometer stations that observed the GMD. Panel d shows that at 05:19 UT, during an interval of very quiet magnetic activity (Figure 10) before the GMD, there were almost no horizontal or vertical currents. At 5:26 an intense, latitudinally localized upward current (red) appeared between Cape Dorset and Salluit, a downward current (blue) extended from the northeast to the northwest of Cape Dorset, and a westward electrojet showed a counterclockwise vortical structure around Cape Dorset. By 5:32 UT the upward current had disappeared, a latitudinally narrow westward electrojet appeared near Salluit, and the region of downward current weakened and moved southward to just north of the electrojet. It is consistent with the lack of significant magnetic variations at INUK and KJPK, shown in the bottom panels of Figure 10, that GOES 13, with its magnetic footpoint near Sanikiluaq, observed only steady levels of energetic electron fluxes and minor variations in the Hp magnetic field component during the entire time interval from 04:00 to 06:00 UT (not shown).

4. Other selected events

Table 3 shows the values of the IMF in GSM coordinates, solar wind velocity (Vsw) in km/s, density (Nsw) in #/cm^3, pressure (Psw) in nPa, and the SML, SMU, and SYM/H magnetic activity indices in nT for the nearly simultaneous DFB – GMD events on six days in 2016 and 2017. The IMF magnitude in all of these events only varied between 3.5 and 10.2 nT with a median of 4.4 nT, and the IMF Bz component varied between -4 and +3 nT, with a median of -1.1 nT. All but one event occurred during intervals of high (≥ 500 km/s) or very high (≥ 650 km/s) Vsw. OMNI data (not shown) indicated that these high Vsw intervals began from 1 to 3 days prior to the DFBs. The only exception (Vsw = 310 km/s) occurred on December 31, 2016 in association with the only high value of Nsw (16.5 #/cc); no magnetic storm followed this event or closely preceded any of the other events. Psw was low or modest in all cases. SML ranged from quiet to moderately disturbed (-54 to -573 nT), with a median of -199 nT. SMU also from ranged from quiet to moderately disturbed (37 to 225 nT), with a median of 68 nT, and SYM/H was consistently quiet, never dropping below -34 nT. These indicate intervals of strong magnetospheric driving (mainly by Vsw) but with little or moderate global magnetospheric response. We note, however, that the lack of any significant global response may be consistent with the generation of fewer DFBs, which might make the occurrence (and hence identification) of temporally and spatially isolated DFBs more likely.

Table 4 shows details of the DFB and GMD events listed in Table 3. Figures documenting each event and including information about substorm onsets near the time of these events (or not) are included in the Supporting Information. Column 2 shows the time the dipolarization front was observed, column 3 shows tsGMD, the start time of the GMD, defined as the first minute showing an increased perturbation in one or more components of the magnetic field at one or more ground stations showing a large GMD, and column 4 shows tpGMD, the time of the peak derivative in any component of the GMD at one or more stations. Columns 5 and 6 show the GSM X and Y velocity components of the DFB, columns 7 and 8 show the GSM X and Y positions of the DFB, and column 9 shows its location in magnetic local time (MLT) in HH:MM.

Figure 12 shows the locations and velocities of each of the DFBs in Table 4 in the X-Y GSM plane. The DFBs were located between -7 and -11 R_E in the -X_{GSM} direction (tailward of Earth), and all but one were within ± 2 R_E and one hour MLT of the midnight meridian. The lines attached to each cross symbol show the direction and relative magnitude of the DFB velocity. The bulk velocity components were generally very small (less than 100 km/s), and much smaller than the ~300 km/s values noted by Runov et al. (2011). This may indicate that the DFBs were significantly decelerated and/or the probe was at a DFB flank and missed the DFB proper. The absolute values of Vx and Vy were also often close, which might signify a flankward flow deflection and/or vorticity. Indeed, it is evident in the summary plots that Vx and Vy often changed their signs, which indicates a flow vortex.

Although on January 27, 2017 both THEMIS probes D and E were located near the PSBL/lobe boundary and encountered a hot plasma sheet expansion at around 0600 UT, the velocities of the DFB observed by THEMIS E at 06:01 UT at -10.4 R_E, 1 R_E tailward of

THEMIS D, did not at all follow the typical pattern in which DFBs have larger earthward velocities when they are observed at larger tailward distances. As shown in Figure S6 in the Supporting Information, Vx was large and negative (at times exceeding -250 km/s) and Vy was positive and even larger (exceeding +300 km/s) during this DFB encounter. The phase delays between the Vx, Vy, and Vz components indicate that THEMIS E encountered a sort of 3-D flow vortex, perhaps related to the passage of the spacecraft in, out, and back again into the plasma sheet. To put this anomalous event in perspective, we note that the DFB simulations shown in Figures 5 and 6 of Birn et al. (2019) included examples of vortex flows with large Vy components.

Figure 13 shows color-coded time delay values for the DFB-GMD events listed in Table 4. Figure 13a shows that the onset time of the GMD preceded the onset of the DFB by ≥ 2 min during eight of the 15 events, preceded it by 1.5 ± 0.5 min during four other events, and preceded it by < 1 min during three events. The mean time delay from GMD onset was 1.83 min and the standard deviation was 1.05 min. The events with larger time delay values generally were observed at X_{GSM} values nearer Earth and nearer local midnight, but with considerable scatter. Figure 13b is similar to Figure 13a, but time delays are from the time of the peak GMD derivative to DFB onset. For this time delay the peak time of the GMD preceded the onset of the DFB by ≥ 2 min during three of the 15 events, coincided in time to within ± 0.5 min during seven events, and followed the onset of the DFB during five events. That is, the peak GMD was approximately simultaneous with the time of the observation of the dipolarization front. The mean time delay from peak GMD was -0.23 min and the standard deviation was 1.31 min.

5. Discussion

Many previous studies have suggested that DFBs are causally related to magnetic disturbances observed by ground magnetometers, but most have focused on their possible contribution to substorm onsets and magnetic bays (Lyons et al., 2012) or global dipolarizations (e.g., the review by Gabrielse et al., 2023) rather than their connection to short-lived but large amplitude GMDs. This paper presents several examples of near-simultaneous DFBs observed by THEMIS spacecraft in the near magnetotail and large amplitude GMDs observed by multiple ground magnetometers located along the east and west coast of Hudson Bay, Canada. Several issues needed to be addressed in order to identify useful events.

First, mapping of magnetic field lines from the near tail to the ground continues to be generally challenging, as empirical models are parameterized by only a few global variables. We addressed this issue by first mapping the northern hemisphere footpoint of the THEMIS spacecraft using the Tsyganenko model T89 (Tsyganenko, 1989) via the SSCWEB utility and selecting any event for which that footpoint was located in eastern Arctic Canada, from ~300 km west of Hudson Bay to the east coast of Labrador. We then looked at ground magnetometer data from the stations shown in Figure 1 to identify large GMDs that occurred near the time of the DFBs. We found that events with footpoints far to the west or east of Hudson Bay did not correspond to any near-simultaneous GMD, and those events with footpoints near the middle of Hudson Bay corresponded to either no events or only weak events. These results are consistent with the 923 km separation distance between Fort Churchill (near the west coast of Hudson Bay) and Inukjuak (on the east coast of Hudson Bay) and the values of the full-width half maximum radii of GMDs of ~275 km reported by Engebretson et al. (2019a) and 250-450 km reported by Weygand et al. (2021). For the two events presented in section 3, we used the Tsyganenko T01 magnetic field model (Tsyganenko, 2002a,b), which included as inputs a "trail" of 5-min averages of the IMF, solar wind, and *Dst* field data, covering the preceding 2-hour interval. The T01 model is known to give more accurate footpoints than T89 (e.g., Nishimura et al., 2011) and our results indicated excellent agreements between the THEMIS footpoints and the ground stations showing the largest GMDs (Figures 5, 6, and 11). Thus we believe that the magnetic footpoints in our work were estimated reasonably.

Second, what relative timing might be expected between DFBs and GMDs? The earthward velocity of DFBs deeper in the magnetotail, averaging 300 km/s near $X_{GSM} = -15\ R_E$, dropped to an average of 180 km/s near $X_{GSM} = -8\ R_E$ (Figure 4b of Liu et al., 2014). Braking of the DFB in the transition region ($X_{GSM} \geq -10\ R_E$) reduces this earthward velocity, sometimes even stopping (Sergeev et al., 2014) or reversing it, and in the process generates a field aligned current pair and destabilizes energetic particles. These can rapidly travel toward the ionosphere to drive the magnetic and auroral signatures observed. The braking process is not instantaneous; momentum is transferred throughout the deceleration. The buildup of plasma ahead of the dipolarization front as the DFB moves earthward has been well documented. The events listed in section 4 all show the initiation of a GMD ~2 min before the observation of the dipolarization front, with a tendency to occur with a larger lead time for events observed nearer Earth – and thus later in the deceleration process. The time delay and its dependence on spacecraft position downtail reported here are therefore consistent with what is known of the braking process.

Third, even though the number of spacecraft in the braking region is quite limited, it is known that many DFBs can occur in a short time interval at slightly different locations. How can one be confident that a given DFB and GMD are related? In particular, what are the typical scale sizes of DFBs, and how do these map to the ground? We use the T01 magnetic field model to address a related inverse question: how does a given set of locations on the ground map to the braking region?

Figure 14 shows the results of mapping a set of five ground locations (BACK and 50 km N, S, E, and W of it) to the GSM X distance tailward where THEMIS D observed a DFB at 5:59 UT January 27, 2017, using the T01 magnetic field model. The cross and diamond symbols in Figure 14a show these five locations, respectively, near the southwest corner of Hudson Bay. Figure 14b shows a mapped projection of the magnetic field lines through these five ground locations on a GSM Z-X grid tailward from the northern ionosphere to the neutral sheet and earthward again toward the southern ionosphere. The location of THEMIS D, shown by the black square, is south of the neutral sheet at X_{GSM} = -9.43 R_E and Z_{GSM} = -3.75 R_E, adjacent to the mapped field line locations south of the neutral sheet near this same X_{GSM} distance. Figure 14c shows a zoomed-in view of the Z_{GSM} and Y_{GSM} locations of THEMIS D and these mapped field lines south of the neutral sheet at this same X_{GSM} distance.

Table 5 presents the Y_{GSM} and Z_{GSM} coordinates of these mapped magnetic field lines at X_{GSM} = -9.43 R_E, the distances of the N, S, E, and W field lines in R_E and km from the mapped BACK field line, and dimensionless mapping factors determined as the ratio between these distances and 50 km.

Liu et al. (2013b) used two methods to infer the radius of DFBs using a data set of 472 earthward traveling DFBs observed by THEMIS spacecraft and concluded that although the radii varied from event to event and could occasionally reach 3 R_E, their median radius was 0.8 – 1.0 R_E. It is not yet known whether the transverse extent of field-aligned currents induced during DFB braking preserves this radius or expands as they are transmitted earthward. Assuming that this radius is preserved, the mean mapping factors of ~32 for longitudinal separations and 62.5

for latitudinal separations together with the median radius of DFBs (0.9 R_E = 5734 km) give estimates of the median radius of DFBs mapped to the ionosphere of 180 km in east-west extent and 90 km in north-south extent. These values are smaller than but of the same order of magnitude as the extent of the localized field-aligned currents shown in Figures 5, 6, and 11, and roughly half of the half amplitude radii of GMDs cited above. Because the sensitivity of ground magnetometers to currents in the ionosphere falls off only gradually with horizontal distances of ~100 km, however, we consider the mapped DFB radii and half amplitude GMD radii to be in reasonable agreement.

Finally, although we are confident that in each of the examples shown a DFB observed at a THEMIS spacecraft is related to a GMD observed nearly simultaneously at two or more closely spaced ground magnetometer stations, the physics underlying that relation is currently only qualitatively understood.

6. Summary and Conclusions

1. As a result of surveying days in 2015-2017 when the apogees of THEMIS A, D, and E were in the midnight sector, one or more DFBs occurred, and the footpoint of the spacecraft's magnetic field in the northern ionosphere were in the longitudinal region surrounding Hudson Bay, we identified six days during which one or more of these DFBs spacecraft coincided closely in time with ≥ 6 nT/s GMDs, observed by latitudinally closely spaced magnetometers near the west or east coasts of Hudson Bay. When the spacecraft were over the middle of Hudson Bay or far to the west or east of it, little or no GMD activity was observed at these ground stations. This is consistent with the results of mapping the spatial extent of DFBs to the ionosphere using the T01 magnetic field model and with our previous observations of the longitudinal extent of GMDs.
2. On two of these days we showed auroral imager data and SECS maps of ionospheric and vertical currents, in each case showing a quiet interval before the DFB and GMD, an interval during the events, and another quiet or nearly quiet interval after the events. In each case the footpoints of two THEMIS spacecraft were very near the ground stations, and a localized intense upward current, a vortical perturbation of a westward electrojet, and an auroral intensification and/or streamers appeared during the DFB and GMD and

disappeared thereafter. These several simultaneous features are consistent with the observations of the auroral drivers of large dB/dt events by Ngwira et al. (2018) and Engebretson et al. (2019), even though their events were selected during geomagnetic storms. Increased levels of energetic electron fluxes observed by GOES 14 shortly after each of the DFB - GMD pairs on January 27 were consistent with auroral activity spatially and temporally independent of the GMDs.

3. All but one of the DFB – GMD pairs during these six days occurred under elevated Vsw and low Nsw and Psw conditions (most above 600 km/s and below 4 cm^{-3} and 3 nPa, respectively). The SYM/H index was above -25 nT for all but one event. The SML and SMU indices showed activity ranging from quiet through moderately disturbed. These external conditions, along with the close temporal association of some but not all of these events with substorm onsets, indicates that they occurred during HILDCAA events, and with essentially no relation to any magnetic storms.
4. GMD onsets during these six days began ~2 min before the time of DFB observation, and GMD peaks occurred nearly simultaneously with them. These time differences most likely reflect the fact that a region of increased plasma pressure typically precedes a DF by 1 min.
5. The earthward velocity (Vx) of the DFBs observed during these six days, at locations in X_{GSM} between -7 and -11 R_E, was with two exceptions lower for events nearer Earth. This is consistent with other DFB observations, and is attributed to braking of the DFBs. The slight increase in the time difference between GMD onsets and DFs observed nearer Earth appears to reflect the fact that the braking of the DFB is not instantaneous: information on the braking may begin to be transferred via field aligned currents and electron precipitation as braking begins but continues as the DFB comes nearer Earth.
6. Additional observations of GMDs and DFBs are certainly warranted, especially in regions with not only dense magnetometer coverage but also with more complete coverage by auroral imagers. We hope, however, that the observations reported here will stimulate modelers to increase their focus on DFBs occurring not only during storm times or the times of substorm onsets, but also during times when large, isolated GMDs occur.

7. Open Research

Ground-based magnetometer data used in this study were recorded at stations in the MACCS (Engebretson et al., 2011), AUTUMNX (Connors et al., 2023), CARISMA (Mann et al., 2023), and CANMOS (Calp, 2023) arrays in Eastern Arctic Canada. The SuperMAG SML and SMU indices accessed in this study are available from the SuperMAG web site (Gjerloev, 2023). THEMIS satellite data and THEMIS all sky imager data are available from the THEMIS web site (Angelopoulos et al., 2023, Mende, 2004). REGO all sky imager data are available from the GO-Canada REGO web site (Donovan, 2014). The GOES-13 and -14 data are available from the NOAA National Centers for Environmental Information (NCEI) (NOAA, 2020, 2023). The Tsyganenko T01 model implementation in IDL (GEOPACK) used in this study was developed by Korth (2020). Field line tracing modules used were accessed via the Space Physics Environment Data Analysis System (SPEDAS) IDL Geopack Library (SPEDAS, 2023)

Acknowledgments

This research was supported by NSF grant AGS-2013648 to Augsburg University, AGS-2013433 to the University of Michigan. Work at the Space Science Institute was supported by NSF grant AGS-2027210 and NASA grant 80NSSC19K0907. Work at UCLA by AR was supported by NASA-LWS grant 80NSSC20K1788, and work by JMW was supported by NASA grants 80NSSC18K0570 and 80NSSC18K1220 and NSF grant AGS-2013648 via subcontract from Augsburg University. Work at Virginia Tech was supported by NSF grants OPP-1744828 and AGS-2027168 and NASA grant 19-LWS19_2-0043. The work of YN was supported by NASA grants 80NSSC20K0725, 80NSSC21K1321, 80NSSC22K0323, 80NSSC22K0749 and 80NSSC23K0410, NSF grants AGS-1907698 and AGS-2100975, and AFOSR grants FA9550-23-1-0614 and FA9550-23-1-0634. The research at the University of Colorado was supported by NOAA cooperative agreements NA17OAR4320101 and NA22OAR4320151. MGC thanks NSERC for research support and the Canadian Space Agency for support of AUTUMNX. IRM was supported by the Natural Sciences and Engineering Research Council of Canada. We thank Ian Mann, D. K. Milling, A. Kale and the rest of the CARISMA team for data. CARISMA is operated by the University of Alberta, funded by the Canadian Space Agency.

We acknowledge NASA contract NAS5-02099 and V. Angelopoulos for use of data from the THEMIS Mission; C.W.~Carlson and J.P.~McFadden for use of ESA data; and D. Larson and R. P. Lin for use of SST data. THEMIS FGM data was provided under the lead of the Technical University of Braunschweig and with financial support through the German Ministry for Economy and Technology and the German Center for Aviation and Space (DLR) under contract 50 OC 0302. The THEMIS and REGO all-sky imagers are supported by NASA NAS5-02099 and the Canada Foundation for Innovation, respectively. We gratefully acknowledge the SuperMAG collaborators (http://supermag.jhuapl.edu/info/?page=acknowledgement). Jesper Gjerloev is SuperMAG Principal Investigator.

Author Contributions

Conceptualization: Mark J. Engebretson, Andrei Runov, Vyacheslav A. Pilipenko, Michael D. Hartinger

Data curation: Mark J. Engebretson, Mark B. Moldwin, Martin G. Connors, Ian R. Mann, Yukitoshi Nishimura, Juan Rodriguez

Formal analysis: Mark J. Engebretson, Andrei Runov, James M. Weygand

Funding acquisition: Mark J. Engebretson

Investigation: Mark J. Engebretson, Sean A. Gaffaney, Jesus A. Ochoa, Andrei Runov, James M. Weygand, Yukitoshi Nishimura, Zhonghua Xu

Methodology: Mark J. Engebretson, Andrei Runov, James M. Weygand, Yukitoshi Nishimura

References:

Amm, O., & Viljanen, A. (1999). Ionospheric disturbance magnetic field continuation from the ground to the ionosphere using spherical elementary currents systems. *Earth Planets and Space*, *51*(6), 431–440. https://doi.org/10.1186/BF03352247

Angelopoulos, V., W. Baumjohann, C. F. Kennel, F. V. Coroniti, M. G. Kivelson, R. Pellat, R. J.Walker, H. Luehr, and G. Paschmann (1992), Bursty bulk flows in the inner central plasma sheet, *Journal of Geophysical Research, 97*, 4027–4039, doi:10.1029/91JA02701.

Angelopoulos, V., C. F. Kennel, F. V. Coroniti, R. Pellat, M. G. Kivelson, R. J. Walker, C. T. Russell, W. Baumjohann, W. C. Feldman, and J. T. Gosling (1994). Statistical characteristics of bursty bulk flow events, *Journal of Geophysical Research*, *99*, 21,257-21,280. https://doi.org/10.1029/94JA01263

Angelopoulos, V. (2008), The THEMIS mission, *Space Sci. Rev, 141*, 5–34. https://doi.org/10.1007/s11214-008-9336-1

Angelopoulos et al., (2023). THEMIS satellite level 2 data. [Dataset]. University of California, Berkeley. http://themis.ssl.berkeley.edu/overview_data.shtml).

Angelopoulos, V. (2023). GITHUB IDL_GEOPACK library. [Software]. https://github.com/spedas-j/spedas_watch/blob/master/idl/external/IDL_GEOPACK/trace/trace2iono.pro

Auster, H.U., Glassmeier, K.H., Magnes, W. et al. (2008). The THEMIS Fluxgate Magnetometer. *Space Sci Rev* **141**, 235–264. https://doi.org/10.1007/s11214-008-9365-9

Birn, J., Liu, J., Runov, A., Kepko, L., & Angelopoulos, V. (2019). On the contribution of dipolarizing flux bundles to the substorm current wedge and to flux and energy transport. *Journal of Geophysical Research: Space Physics, 124,* 5408–5420. https://doi.org/10.1029/2019JA026658

Califf, S., Rich, F. J., Loto'aniu, T. M., Singer, H. J., & Redmon, R. J., (2023). Long-term Bias Stability of the GOES-NOP Magnetometers, *Earth and Space Science,* accepted October 2023.

Calp, D. (2023). Canadian Magnetic Observatory System (CANMOS) Data. [Dataset]. Natural Resources Canada, Ottawa, Canada. http://geomag.nrcan.gc.ca/data-donnee/sd-en.php.

Connors, M., Schofield, I., Reiter, K., Chi, P. J., Rowe, K. M., & Russell, C. T. (2016). The AUTUMNX magnetometer meridian chain in Quebec, Canada. *Earth, Planets and Space*, *68*. https://doi.org/10.1186/s40623-015-0354-4

Connors, M. G. (2023). AUTUMNX Athabasca University THEMIS UCLA Magnetometer Network. [Dataset]. Athabasca University, Canada. https://autumn.athabascau.ca

Donovan, E., Mende, S. B., Jackel, B., Frey, H. U., Syrjäsuo, M., Voronkov, I., Trondsen, T., Peticolas, L. M., Angelopoulos, V., Harris, S. E., Greffen, M., and Connors, M. G. (2006). The THEMIS all-sky imaging array—System design and initial results from the prototype imager. *Journal of Atmospheric and Solar-Terrestrial Physics, 68(13*), 1472-1487. https://doi.org/10.1016/j.jastp.2005.03.027

Donovan, E. (2014) REGO all sky imager data. [Dataset]. University of Calgary, Canada. https://data.phys.ucalgary.ca/sort_by_instrument/all_sky_camera/GO-Canada_REGO/stream0

Engebretson, M. J., Hughes, W. J., Alford, J. L., Zesta, E., Cahill, L. J., Jr., Arnoldy, R. L., & Reeves, G. D. (1995). Magnetometer array for cusp and cleft studies observations of the spatial extent of broadband ULF magnetic pulsations at cusp/cleft latitudes. *Journal of Geophysical Research*, *100*, 19371–19386. https://doi.org/10.1029/95JA00768

Engebretson, M., Steinmetz, E., & Moldwin, M. (2011). MACCS 0.5 s Ground Magnetometer Data. [Dataset]. Augsburg University. https://doi.org/10.48322/sydj-ab90

Engebretson, M. J., Pilipenko, V. A., Ahmed, L. Y., Posch, J. L., Steinmetz, E. S., Moldwin, M. B., Connors, M. G., Weygand, J. M., Mann, I. R., Boteler, D. H., Russell, C. T., & Vorobev, A. V. (2019a). Nighttime magnetic perturbation events observed in Arctic Canada: 1. Survey and statistical analysis. *Journal of Geophysical Research: Space Physics*, *124*, 7442-7458. https://doi.org/10.1029/2019JA026794

Engebretson, M. J., Steinmetz, E. S., Posch, J. L., Pilipenko, V. A., Moldwin, M. B., Connors, M. G., Boteler, D. H., Mann, I. R., Hartinger, M. D., Weygand, J. M., Lyons, L. R., Nishimura, Y., Singer, H. J., Ohtani, S., Russell, C. T., Fazakerley, A., & Kistler, L. M. (2019b). Nighttime magnetic perturbation events observed in Arctic Canada: 2. Multiple-instrument observations. *Journal of Geophysical Research: Space Physics*, *124*, 7459-7476. https://doi.org/10.1029/2019JA026797

Engebretson, M. J., Pilipenko, V. A., Steinmetz, E. S., Moldwin, M. B., Connors, M. G., Boteler, D. H., Singer, H. J., Opgenoorth, H., Schillings, A., Ohtani, S., Gjerloev, J., and Russell, C. T. (2021a). Nighttime magnetic perturbation events observed in Arctic Canada: 3. Occurrence and amplitude as functions of magnetic latitude, local time, and magnetic disturbances. *Space Weather*, *19*, e2020SW002526. https://doi.org/10.1029/2020SW002526

Engebretson, M. J., Ahmed, L. Y., Pilipenko, V. A., Steinmetz, E. S., Mark B. Moldwin, Martin G. Connors, David H. Boteler, James M. Weygand, Shane Coyle, Shin Ohtani, Jesper Gjerloev, and Christopher T. Russell (2021b). Superposed epoch analysis of nighttime magnetic perturbation events observed in Arctic Canada. *Journal of Geophysical Research: Space Physics*, *126*, e2021JA029465. https://doi:10.1029/2021JA029465

Engebretson, M. J., Yang, L., Steinmetz, E. S., Pilipenko, V. A., Moldwin, M. B., McCuen, B. A., Connors, M. G., Weygand, J. M., Waters, C. L., Nishimura, Y., Lyons, L. R., & Russell, C. T. (2023). Extreme Geomagnetic Disturbances (GMDs) Observed in Eastern Arctic Canada: Occurrence Characteristics and Solar Cycle Dependence. Submitted to the *Journal of Geophysical Research: Space Physics*, April 15, 2023. https://doi:10.1029/2023JA031643R

Forsyth, C., Rae, I. J., Coxon, J. C., Freeman, M. P., Jackman, C. M., Gjerloev, J., & Fazakerley, A. N. (2015). A new technique for determining Substorm Onsets and Phases from Indices of the Electrojet (SOPHIE). *J. Geophys. Res. Space Physics*, *120*, 10,592–10,606. https://doi.org/10.1002/2015JA021343

Forsyth, C. Sergeev, V. A., Henderson, M. G., Nishimura, Y., & Gallardo-Lacourt, B. (2020). Physical Processes of Meso-Scale, Dynamic Auroral Forms. *Space Science Reviews, 216:46*. https://doi.org/10.1007/s11214-020-00665-y

Gabrielse, C., Gkioulidou, M., Merkin, S., Malaspina, D., Turner, D.L., Chen, M.W., Ohtani, S-I., Nishimura, Y., Liu, J., Birn, J., Deng, Y., Runov, A., McPherron, R.L., Keesee, A., Yin Lui, A.T., Sheng, C., Hudson, M., Gallardo-Lacourt, B., Angelopoulos, V., Lyons, L., Wang, C.-P., Spanswick, E. L., Donovan, E., Kaeppler, S.R., Sorathia, K., Kepko, L., and Zou, S, (2023), Mesoscale phenomena and their contribution to the global response: a focus on the magnetotail transition region and magnetosphere-ionosphere coupling. *Frontiers in Astronomy and Space Science* 10:1151339. doi: 10.3389/fspas.2023.1151339

Gjerloev, J. W. (2023). SuperMAG, Global magnetic field observations and products made possible by the contributors. [Dataset]. Applied Physics Laboratory. https://supermag.jhuapl.edu/

Hanser, F. (2011). *EPS/HEPAD calibration and data handbook*. Assurance Technology Corporation. https://www.ngdc.noaa.gov/stp/satellite/goes/doc/goes_nop/GOESN-ENG-048_RevD_EPS_HEPAD_13May2011.pdf

Jaynes, A. N., Lessard, M. R., Rodriguez, J. V., Donovan, E., Loto'aniu, T. M., and Rychert, K. (2013). Pulsating auroral electron flux modulations in the equatorial magnetosphere. *Journal of Geophysical Research: Space Physics, 118,* 4884–4894. https://doi:10.1002/jgra.50434.

Korth, H. (2020). IDL GEOPACK Dynamic Link Module: April 8, 2020 Release (Version 10.6). [Software]. Applied Physics Laboratory. https://ampere.jhuapl.edu/tools/

Li, S.-S., V. Angelopoulos, A. Runov, X.-Z. Zhou, J. P. McFadden, D. Larson, J. Bonnell, and U. Auster (2011), On the force balance around dipolarization fronts within bursty bulk flows. *Journal of Geophysical Research, 116,* A00I35. https://doi:10.1029/2010JA015884

Liu, J., Angelopoulos, V., Runov, A., & Zhou, X.-Z. (2013a). On the current sheets surrounding dipolarizing flux bundles in the magnetotail: The case for wedgelets. *Journal of Geophysical Research: Space Physics, 118,* 2000–2020. https://doi.org/10.1002/jgra.50092

Liu, J., Angelopoulos, V., Zhou, X.-Z., Runov, A., & Yao, Z. (2013b). On the role of pressure and flow perturbations around dipolarizing flux bundles. *Journal of Geophysical Research: Space Physics, 118,* 7104–7118. https://doi.org/10.1002/2013JA019256

Liu, J., Angelopoulos, V., Zhou, X.-Z., & Runov, A. (2014). Magnetic flux transport by dipolarizing flux bundles. *Journal of Geophysical Research: Space Physics, 119,* 909–926. https://doi.org/10.1002/2013JA019395

Liu, J., Angelopoulos, V., Zhang, X.-J., Runov, A., Artemyev, A., Plaschke, Fu, S, Lu, S., Yi-Hsin Liu, & Chu, X. (2017). Ultralow frequency waves deep inside the inner magnetosphere driven by dipolarizing flux bundles. *Journal of Geophysical Research: Space Physics, 122,* 10,112–10,128. https://doi.org/10.1002/2017JA024270

Lyons, L. R., Nishimura,Y., Xing, X., Runov,A., Angelopoulos,V., Donovan, E., & and T. Kikuchi, T. (2012). Coupling of dipolarization front flow bursts to substorm expansion phase phenomena within the magnetosphere and ionosphere. *Journal of Geophysical Research, 117,* A02212. https://doi:10.1029/2011JA017265

Lyons, L. R., Gallardo-Lacourt, B., & Nishimura, Y (2022). Chapter 2 - Auroral structures: Revealing the importance of meso-scale M-I coupling, in *Cross-Scale Coupling and Energy Transfer in the Magnetosphere-Ionosphere-Thermosphere System,* edited by Y. Nishimura, O. Verkhoglyadova, Y. Deng, and S.-R. Zhang, 65-101. Elsevier, Amsterdam, Netherlands. https://doi.org/10.1016/C2019-0-00526-2

Mann, I. R., Milling, D. K., Rae, I. J., Ozeke, L. G., Kale, A., Kale, Z. C., et al. (2008). The upgraded CARISMA magnetometer array in the THEMIS era. *Space Science Reviews, 141*(1-4), 413–451. https://doi.org/10.1007/s11214-008-9457-6

Mann, I.R., Milling, D.K. and Kale, A. (2023). CARISMA Magnetometer Network. [Dataset]. University of Alberta, Canada. https://carisma.ca

McFadden, J.P., Carlson, C.W., Larson, D. et al. (2008). The THEMIS ESA Plasma Instrument and In-flight Calibration. *Space Sci Rev* **141**, 277–302. https://doi.org/10.1007/s11214-008-9440-2

Mende, S. B. (2004). THEMIS all sky imager data. [Dataset]. University of California, Berkeley. http://themis.ssl.berkeley.edu/themisdata/thg/l1/asi/

Mende, S. B., Harris, S. E., Frey, H. U., Angelopoulos, V., Russell, C. T., Donovan, E., Jackel, B., Greffen, M., and Peticolas, L. M. (2008). The THEMIS array of ground-based observatories for the study of auroral substorms. *Space Science Reviews, 141*, 357. https://doi.org/10.1007/978-0-387-89820-9_16

Nakamura, R., Baumjohann, W., Schödel, R., Brittnacher, M., Sergeev, V. A., Kubyshkina, M., Mukai, T., & Liou, K. (2001). Earthward flow bursts, auroral streamers, and small expansions. *Journal of Geophysical* Research, 106, 10,791–10,802. https://doi.org/10.1029/2000JA000306

Newell, P. T., and J. W. Gjerloev (2011a), Evaluation of SuperMAG auroralelectrojet indices as indicators of substorms and auroral power. *Journal of Geophysical Research ,116,* A12211, doi:10.1029/2011JA016779

Ngwira C. M., Sibeck, D., Silveira, M. D. V., Georgiou, M., Weygand, J. M., Nishimura, Y., & Hampton, D. (2018). A study of intense local d*B*⁄dt variations during two geomagnetic storms. *Space Weather*, *16*, 676–693. https://doi.org/10.1029/2018SW001911

Nishimura, Y., Bortnik, J., Li, W., Thorne, R. M., Lyons, L. R., Angelopoulos, V., Mende, S. B., Bonnell, J., Le Contel, O., Cully, C., Ergun, R., and Auster, U. (2011). Estimation of magnetic field mapping accuracy using the pulsating aurora-chorus connection. *Geophysical Research Letters, 38*, L14110, https:doi:10.1029/2011GL048281

Nikitina, L., Trichtchenko, L., & Boteler, D. H. (2016). Assessment of extreme values in geomagnetic and geoelectric field variations for Canada. *Space Weather, 14,* 481–494. https://doi.org/10.1002/2016SW001386

NOAA (2020). GOES 1-15 Space Weather Instruments, Energetic Particle Sensor (EPS), Operational Data, [Dataset] National Centers for Environmental Information, Boulder, Colorado. https://www.ncei.noaa.gov/data/goes-space-environment-monitor/access/avg/

NOAA (2023). GOES 1-15 Space Weather Instruments, Magnetic Fields, Science Quality Data. [Dataset] National Centers for Environmental Information, Boulder, Colorado. https://www.ncei.noaa.gov/data/goes-space-environment-monitor/access/science/mag/

Ohtani, S. I., M. A. Shay, and T. Mukai (2004), Temporal structure of the fast convective flow in the plasma sheet: Comparison between observations and two-fluid simulations, *Journal of Geophysical Research Letters, 109,* A03210. https://doi:10.1029/2003JA010002

Ohtani, S., & Gjerloev, J. W. (2020). Is the substorm current wedge an ensemble of wedgelets?: Revisit to midlatitude positive bays. *Journal of Geophysical Research: Space Physics*, *125,* e2020JA027902. https://doi.org/10.1029/2020JA027902

Panov, E. V., Nakamura, R., Baumjohann, W., Angelopoulos, V., Petrukovich, A. A., Retinò, R., Volwerk, M., Takada, T., Glassmeier, K.-H. , McFadden, J. P., & Larson, D. (2010). Multiple overshoot and rebound of a bursty bulk flow. *Geophysical Research Letters, 37,* L08103, https://doi:10.1029/2009GL041971

Panov, E. V., Kubyshkina, M. V., Nakamura, R., Wolfgang Baumjohann, W., Angelopoulos, V., Sergeev, V. A., & Petrukovich, A. A. (2013). Oscillatory flow braking in the magnetotail: THEMIS statistics. *Geophysical Research Letters, 40,* 2505-2510. https://doi:10.1002/grl.50407

Rodriguez, J. V. (2014). GOES 13-15 MAGE/PD Pitch Angles Algorithm Theoretical Basis Document, Version 1.0, available at: https://www.ngdc.noaa.gov/stp/satellite/goes/doc/MAGEPD_PitchAngles_Processing_ATBD_v1.0.pdf

Runov, A., Angelopoulos, V., Sitnov, M. I., Sergeev, V. A., Bonnell, J., McFadden, J. P., … Auster, U. (2009). THEMIS observations of an earthward-propagating dipolarization front. *Geophysical Research Letters, 36,* L14106. https://doi.org/10.1029/2009GL038980

Runov, A., V. Angelopoulos, M. Sitnov, V.A. Sergeev, R. Nakamura, Y. Nishimura, H.U. Frey, J.P. McFadden, D. Larson, J. Bonnell, K.-H. Glassmeier, U. Auster, M. Connors, C.T. Russell, and H.J. Singer (2011). Dipolarization fronts in the magnetotail plasma sheet. *Planetary and Space Science, 59*, 517-525. https://doi.org/10.1016/j.pss.2010.06.006

Runov, A., Angelopoulos, V., & Zhou, X.-Z. (2012). Multipoint observations of dipolarization front formation by magnetotail reconnection. *Journal of Geophysical Research: Space Physics 117,* A05230. doi:10.1029/2011JA017361.

Sergeev, V. A., Nikolaev, A. V., Tsyganenko, N. A., Angelopoulos, V., Runov, A. V., Singer, H. J., & Yang, J. (2014). Testing a two-loop pattern of the substorm current wedge (SCW2L). *Journal of Geophysical Research: Space Physics*, *119*, 947–963. https://doi.org/10.1002/2013JA019629.

Sergeev, V. A., Sauvaud, J.A., Popescu, D., Kovrazhkin, R. A., Liou, K., Newell, P. T., Brittnacher, M., Parks, G., Nakarnura, R., Mukai, T., & Reeves, G. D. (2000a). Multiple-spacecraft observation of a narrow transient plasma jet in the Earth's plasma sheet. *Geophysical Research Letters, 27*, 851-854. https://doi.org/10.1029/1999GL010729

Sergeev, V. A., Sauvaud, J.-A., Popescu, D., Kovrazhkin, R. A., Lutsenko, V. N., Zelenyi, L. M., Syrjäsuo, M., Viljanen, A., Pulkkinen, T.I., Kudela, K., Kokubun, S., &Mukai, T. (2000b). Plasma sheet ion injections into the auroral bulge: correlative study of spacecraft and ground observations. *Journal of Geophysical Research, 105,* 18465–18482. https://doi.org/10.1029/1999JA900435

Sibeck, D. G., and V. Angelopoulos (2008), THEMIS science objectives and mission phases, *Space Science Reviews, 141,* 35–59. https://doi.org/10.1007/s11214-008-9393-5

Sillanpää, I., Ganushkina, N. Y., Dubyagin, S., & Rodriguez, J. V. (2017). Electron fluxes at geostationary orbit from GOES MAGED data. *Space Weather*, 15, 1602–1614. https://doi.org/10.1002/2017SW001698

Tsurutani, B. T., & Gonzalez. W. D. (1987). The cause of high intensity long duration continuous AE activity (HILDCAAs): Interplanetary Alfven wave trains. *Planetary and Space Science., 35,* 405–412. https://doi.org/10.1016/0032-0633(87)90097-3

Tsurutani, B. T., Gonzalez, W. D., Gonzalez, A. L. C., Tang, F., Arballo, J. K., & Okada, M. (1995). Interplanetary origin of geomagnetic activity in the declining phase of the solar cycle. *Journal of Geophysical Research, 100, A11.* https://doi.org/10.1029/95JA01476

Tsyganenko, N. A. (1989). A magnetospheric magnetic field model with a warped tail current sheet. *Planetary and Space Science*, *37*, 5–20. https://doi.org/10.1016/0032-0633(89)90066-4

Tsyganenko, N. A. (2002a). A model of the near magnetosphere with a dawn-dusk asymmetry, 1. Mathematical structure. *Journal of Geophysical Research*, 107(A8). http://doi.org/10.1029/2001JA000219

Tsyganenko, N. A. (2002b). A model of the near magnetosphere with a dawn-dusk asymmetry, 2. Parameterization and fitting to observations. *Journal of Geophysical Research,* 107(A8). http://doi.org/10.1029/2001JA000220

Weygand, J. M. (2009a). *Equivalent Ionospheric Currents (EICs) derived using the Spherical Elementary Currrent Systems (SECS) technique at 10 s Resolution in Geographic Coordinates*. University of California. https://doi.org/10.21978/P8D62B

Weygand, J. M. (2009b). *Spherical Elementary Current (SEC) Amplitudes derived using the Spherical Elementary Currents Systems (SECS) technique at 10 sec Resolution in Geographic Coordinates*. UCLA. https://doi.org/10.21978/P8PP8X

Weygand, J. M., Amm, O., Viljanen, A., Angelopoulos, V., Murr, D., Engebretson, M. J., et al. (2011). Application and validation of the spherical elementary currents systems technique for deriving ionospheric equivalent currents with the North American and Greenland ground magnetometer arrays. *Journal of Geophysical Research*, *116*, A03305. https://doi.org/10.1029/2010JA016177

Weygand, J. M., Engebretson, M. J., Pilipenko, V. A., Steinmetz, E. S., Moldwin, M. B., Connors, M. G., Nishimura, Y., Lyons, L. R., Russell, C. T., Ohtani, S., and Gjerloev, J. (2021), SECS analysis of nighttime magnetic perturbation events observed in Arctic Canada, *Journal of Geophysical Research: Space Physics*, *126*, e2021JA029839, doi:10.1029/2021JA029839

Weygand, J. M., Bortnik, J., Chu, X., Cao, X., Li, J., Aryan, H., & Tian, S. (2022). Magnetosphere-ionosphere coupling between north-south propagating streamers and high-speed earthward flows. *Journal of Geophysical Research: Space Physics*, *127*, e2022JA030741. https://doi.org/10.1029/2022JA030741

Zhou, X.-Z., V. Angelopoulos, V. A. Sergeev, and A. Runov (2010). Accelerated ions ahead of earthward propagating dipolarization fronts. *Journal of Geophysical Research*, *115,* A00I03. https://doi:10.1029/2010JA015481

Zhou, X.-Z., V. Angelopoulos, V. A. Sergeev, and A. Runov (2011). On the nature of precursor flows upstream of advancing dipolarization fronts, *Journal of Geophysical Research*, *116*, A03222. https://doi:10.1029/2010JA016165

Zou, Y., Dowell, C., Ferdousi, B., Lyons, L. R., & Liu, J. (2022). Auroral drivers of large dB/dt during geomagnetic storms. *Space Weather*, *20*, e2022SW003121. https://doi.org/10.1029/2022SW003121

Table 1. Ground-based magnetometers used in this study. Corrected magnetic (CGM) coordinates are for January 1, 2017 using http://sdnet.thayer.dartmouth.edu/aacgm/aacgm_calc.php#AACGM.

Array	Station	Code	Geog. Lat.	Geog. Lon.	CGM Lat.	CGM Lon.	Cadence
MACCS	Cape Dorset	CDR	64.2°	283.4°	72.6°	2.8°	0.5 s
AUTUMNX	Salluit	SALU	62.2°	284.4°	70.6°	4.1°	0.5 s
	Puvurnituq	PUVR	60.0°	282.7°	68.7°	1.2°	0.5 s
	Inukjuak	INUK	58.5°	281.9°	67.4°	0.0°	0.5 s
	Kuujuarapik	KJPK	55.3°	282.3°	64.3°	0.3°	0.5 s
	Radisson	RADI	53.8°	282.4°	62.8°	0.3°	0.5 s
CANMOS	Sanikiluaq	SNK	56.5°	280.8°	65.5°	-1.9°	1.0 s
CARISMA	Rankin Inlet	RANK	62.8°	267.9°	71.6°	-22.2°	1.0 s
	Fort Churchill	FCHU	58.8°	265.9°	67.8°	-24.8°	1.0 s
	Back Lake	BACK	57.7°	265.8°	66.8°	-24.8°	1.0 s
	Gillam	GILL	56.4°	265.4°	65.5°	-25.3°	1.0 s

Table 2. Geographic distances between adjacent pairs of magnetometer stations along the west and east coast of Hudson Bay, respectively.

Station Pair	Distance (km)	Station Pair	Distance (km)
RANK – FCHU	458	CDR – SALU	228
FCHU – BACK	123	SALU – PUVR	261
BACK – GILL	147	PUVR – INUK	173
		INUK – KJPK	356
		KJPK - RADI	167

Table 3. Solar Wind, interplanetary magnetic field, and global magnetic activity indices during 6 selected days. Omni data solar wind and IMF data were unavailable during 2-hour and 4-hour intervals surrounding the events on January 7 and February 5, 2017, respectively. Time-shifted ARTEMIS P2 data were substituted for January 7, and time-shifted WIND data for February 5 and for Psw on January 7.

Date	Time	IMF |B|	GSM IMF Bx	GSM IMF By	GSM IMF Bz	Vsw	Nsw	Psw	SML	SMU	SYM/H
12/26/2016	3:31	5.1	-2	4.5	-2.4	690	3.7	3.55	-314	133	-23
12/26/2016	5:18	5.3	-2.7	-1.3	-4	675	3.4	3.05	-239	79	-34
12/31/2016	4:45	5.7	-4.7	2.4	-1.6	310	16.5	3.05	-54	37	6
1/7/2017	4:53	3.8	-0.7	-1.9	-3.2	697	2.4	1.8	-199	53	-15
	5:11	4.0	-0.8	-3.4	-1.9	696	2.0	1.7	-174	55	-17
	5:27	4.8	-2.8	-3.7	-1.3	662	1.9	1.6	-240	182	-17
	4:51	4.0	-1.7	1.4	-3.3	707	2.8	2.0	-280	53	-14
	5:09	4.0	-1.6	-3.6	-0.7	693	1.7	1.7	-97	107	-17
	5:25	5.2	-2.1	-3.9	-2.8	689	2.4	1.9	-198	186	-17
1/19/2017	5:26	5.8	-2.7	4.5	1	600	3.9	2.8	-173	40	-24
	5:27	5.7	-2.5	4.4	1.2	593	3.9	2.7	-186	46	-24
1/27/2017	5:47	10.2	-7.7	1.7	6.2	631	6.8	5.4	-488	133	-16
	6:00	7.7	-2.7	3.4	2.1	637	6.8	5.5	-573	221	-19
	6:01	9.2	-3.5	2.5	6.7	629	6.7	5.3	-558	225	-19
2/5/2017	3:18	~6.1	~3	~-5.2	~-1.6	~500	~7	~2.9	-137	171	-21

Table 4. DFB and near-simultaneous GMD event times and DFB locations and velocities during 6 selected days.

Date	S/C	tDFB	tsGMD	tpGMD	Vx	Vy	X (R_E)	Y(R_E)	MLT
12/26/2016	A	3:30:51	3:30	3:32	5.4	3.9	-8.03	-0.12	0:03
12/26/2016	D	5:17:35	5:16	5:18	-4.2	10.7	-7.34	-1.55	0:43
12/31/2016	D	4:46:47	4:44	4:45	5	63.1	-7.17	-0.49	0:14
1/7/2017	D	4:53:31	4:51	4:52	-2.8	15.8	-7.69	0.08	23:58
	D	5:11:11	5:08	5:09	10	15.9	-7.94	-0.18	0:05
	D	5:26:58	5:23	5:27	1.2	25.5	-8.18	-0.43	0:11
	E	4:51:27	4:51	4:52	-8	21.3	-8.76	-1.08	0:25
	E	5:09:20	5:08	5:09	28.4	-6.5	-8.93	-1.35	0:31
	E	5:25:12	5:23	5:27	30.7	103.3	-9.08	-1.6	0:36
1/19/2017	D	5:26:16	5:25	5:27	39.4	46.3	-8.74	1.01	23:34
	E	5:27:08	5:25	5:27	108.6	84.2	-9.75	-0.02	0:01
1/27/2017	D	5:46:58	5:45	5:48	-28.4	-4.3	-9.31	1.77	23:20
	D	5:59:23	5:59	6:02	43.5	-45.4	-9.44	1.66	23:23
	E	6:01:20	5:59	6:02	-91.6	76.5	-10.4	0.66	0:46
2/5/2017	E	3:17:52	3:16	3:17	11.2	-23.6	-8.73	3.56	22:35

Table 5. Mapped locations in GSM coordinates of magnetic field lines from 50 km N, S, E, and W of BACK to the X_{GSM} location of THEMIS D at 5:59 UT January 27, 2017, distance between the mapped N, S, E, and W field lines and the location of the mapped BACK field line, and the resulting ground-to space mapping factors.

Station	N		S		E		W		BACK	
	Y	Z	Y	Z	Y	Z	Y	Z	Y	Z
Locations (R_E)	0.89	-4.54	1.17	-3.61	0.75	-4.23	1.23	-4.11	0.99	-4.17
Distance to BACK (R_E)	0.384		0.600		0.245		0.253		0	
Distance to BACK (km)	2452		3802		1561		1609		0	
Scale mapping factors	49.0		76.0		31.2		32.2			

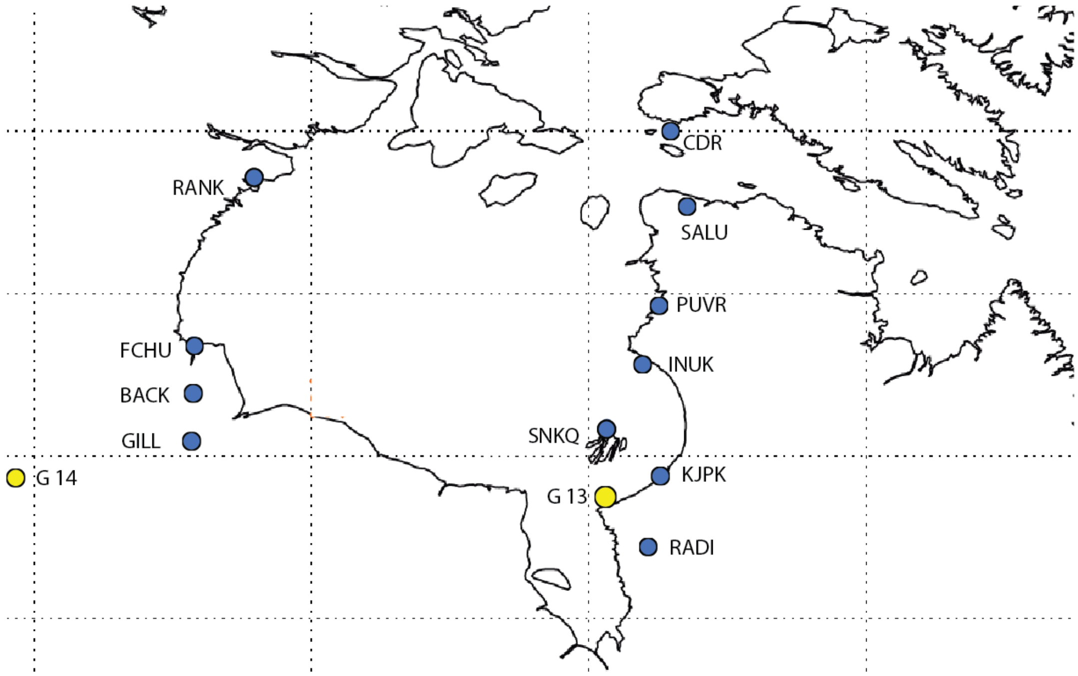

Figure 1. Map of the Hudson Bay region in Arctic Canada showing ground magnetometer stations used for this study (blue circles) and the magnetic footpoints of GOES 13 and 14 at 0600 UT January 27, 2017 (yellow circles).

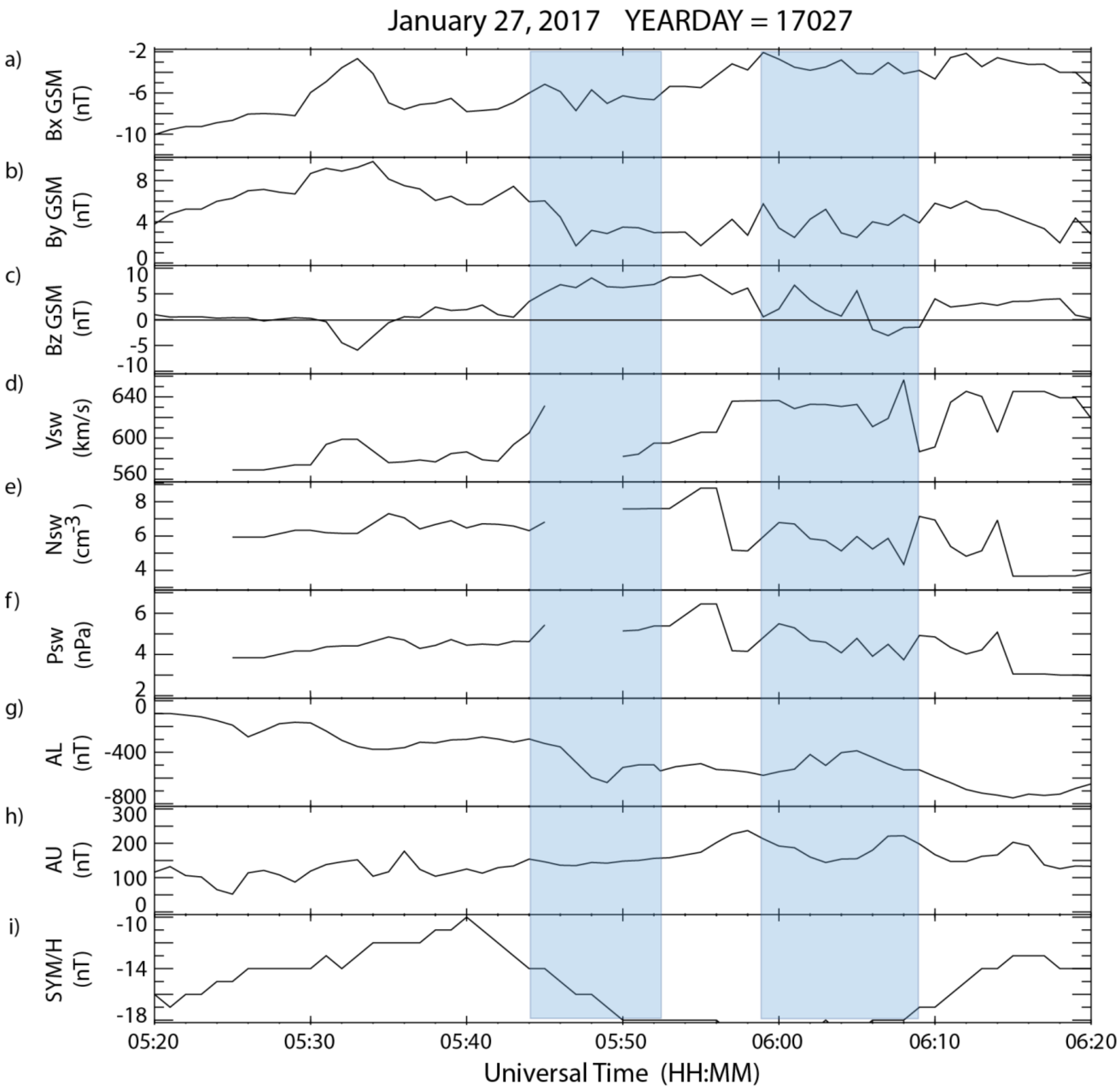

Figure 2. Time-shifted OMNI IMF and solar wind data (panels a-f) and the AL, AU, and SYM/H magnetic activity indices (panels g-i) from 05:20 to 06:20 UT January 27, 2017. The two shaded intervals show time intervals with nearly simultaneous DFBs observed by THEMIS D and GMDs observed by four ground magnetometers located along the west coast of Hudson Bay.

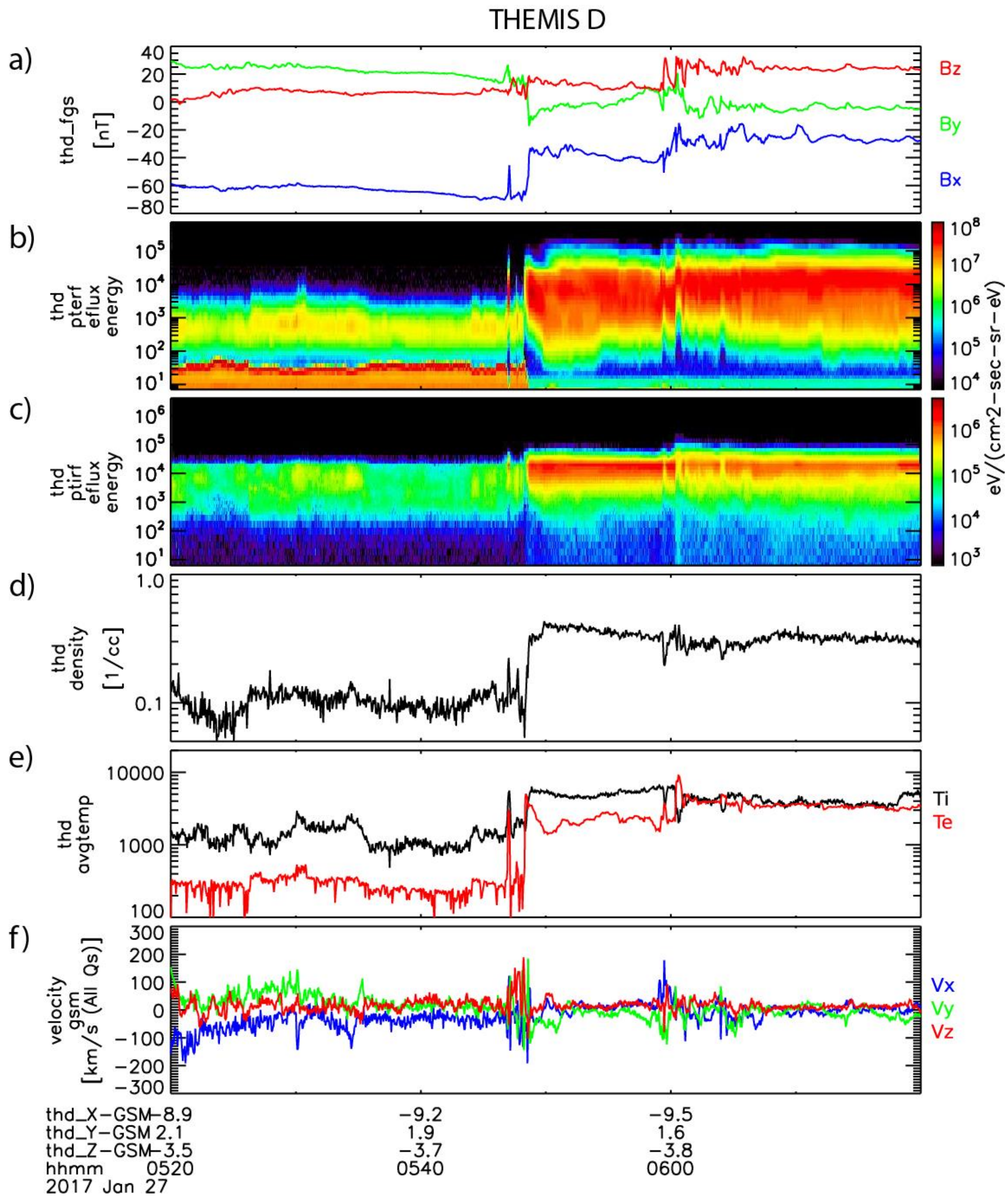

Figure 3. THEMIS D overview from 05:20 to 06:20 UT January 27, 2017. Panel a shows the three components of the magnetic field in GSM coordinates. Panels b and c are omnidirectional energy flux spectra of the differential energy flux of electrons and ions, respectively. Panels d and e show the ion density and ion (black) and electron (red) temperatures, respectively, and panel f shows the three components of the ion flow in GSM coordinates.

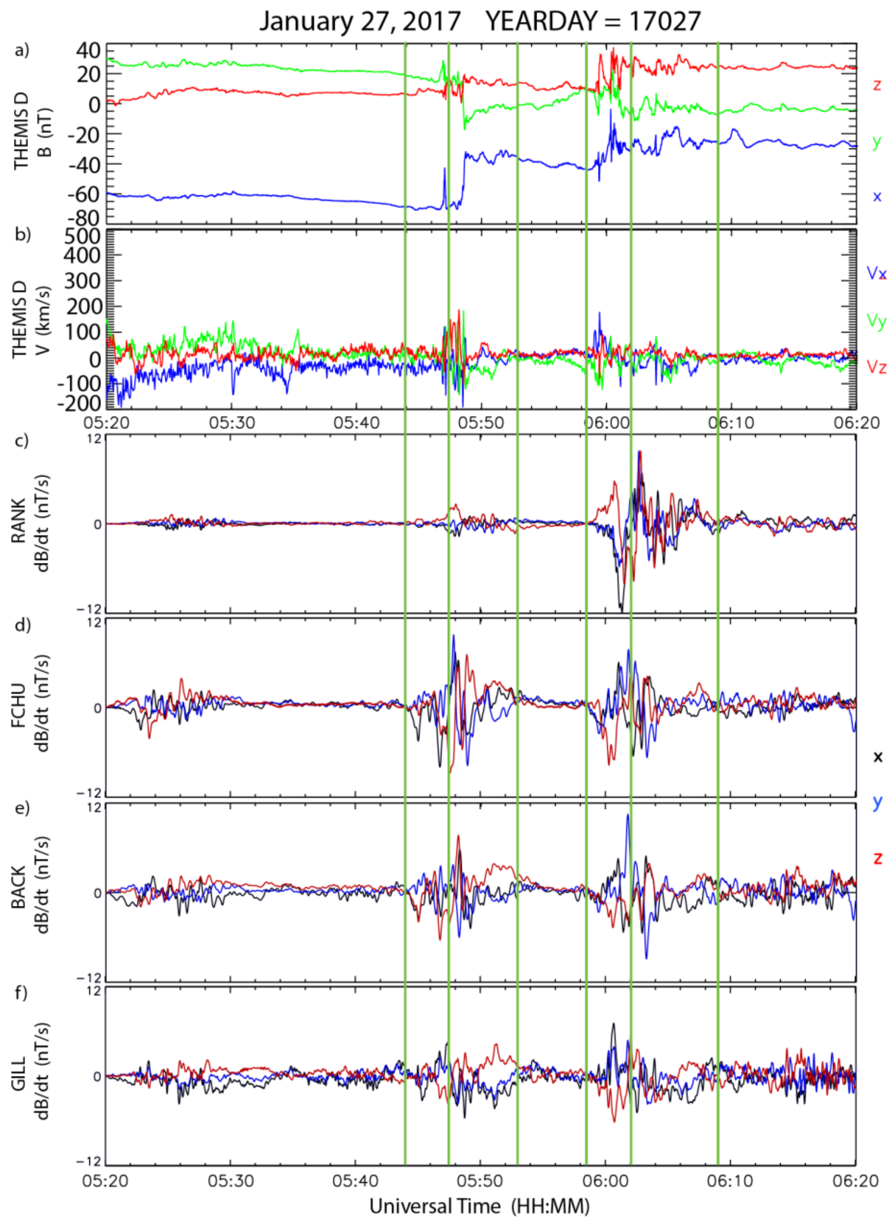

Figure 4. Composite plot showing simultaneous observations of the magnetic field and bulk velocity observed by THEMIS-D and the magnetic field observed by four ground-based magnetometers, in order of decreasing latitude, from 05:20 to 06:20 UT January 27, 2017. Panels a and b show the GSM vector components of the magnetic field and bulk velocity observed by THEMIS-D. Panels c, d, e, and f show three components of the time derivative of the magnetic field from Rankin Inlet, Fort Churchill, Back, and Gillam, respectively, in local geomagnetic coordinates. The vertical green lines correspond to the times of SECS maps and composite all-sky images shown in Figures 5 and 6.

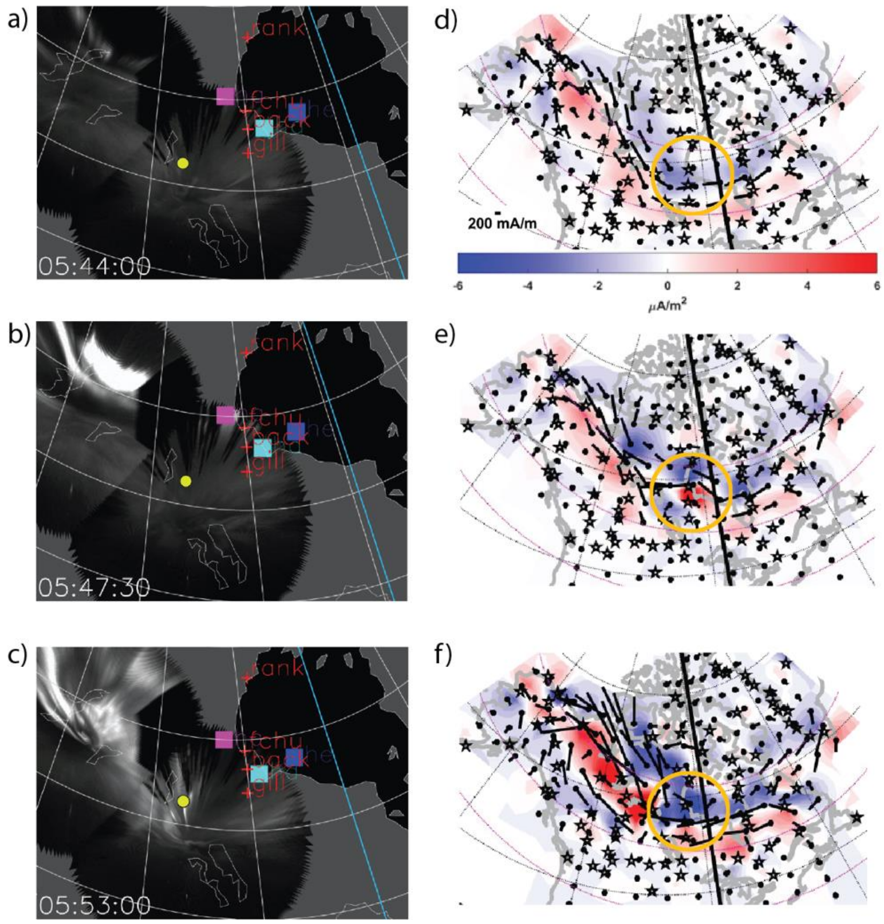

Figure 5. Simultaneous auroral images and SECS maps at times before, during, and after the first DFB-GMD event shown in Figure 4. Panels a, b, and c show composite all-sky auroral images at 05:44, 05:47:30, and 05:53 UT, respectively, on January 27, 2017. The pink, aqua, and blue squares denote the footpoints of THEMIS-A, -D, and -E, respectively. The locations of RANK, FCHU, BACK, and GILL near the western edge of Hudson Bay are shown by red crosses. The yellow dot shows the magnetic footpoint of GOES 14. Panels d, e, and f are maps at these same times of the equivalent ionospheric currents (black arrows) and vertical current intensities (upward in red, downward in blue) across northern North America and Greenland produced using the Spherical Elementary Current Systems method. The stars inside the yellow circle in each SECS image correspond to the locations of the magnetometer stations. The scale for the ionospheric currents and the color bar for the vertical currents are shown at the bottom of panel d.

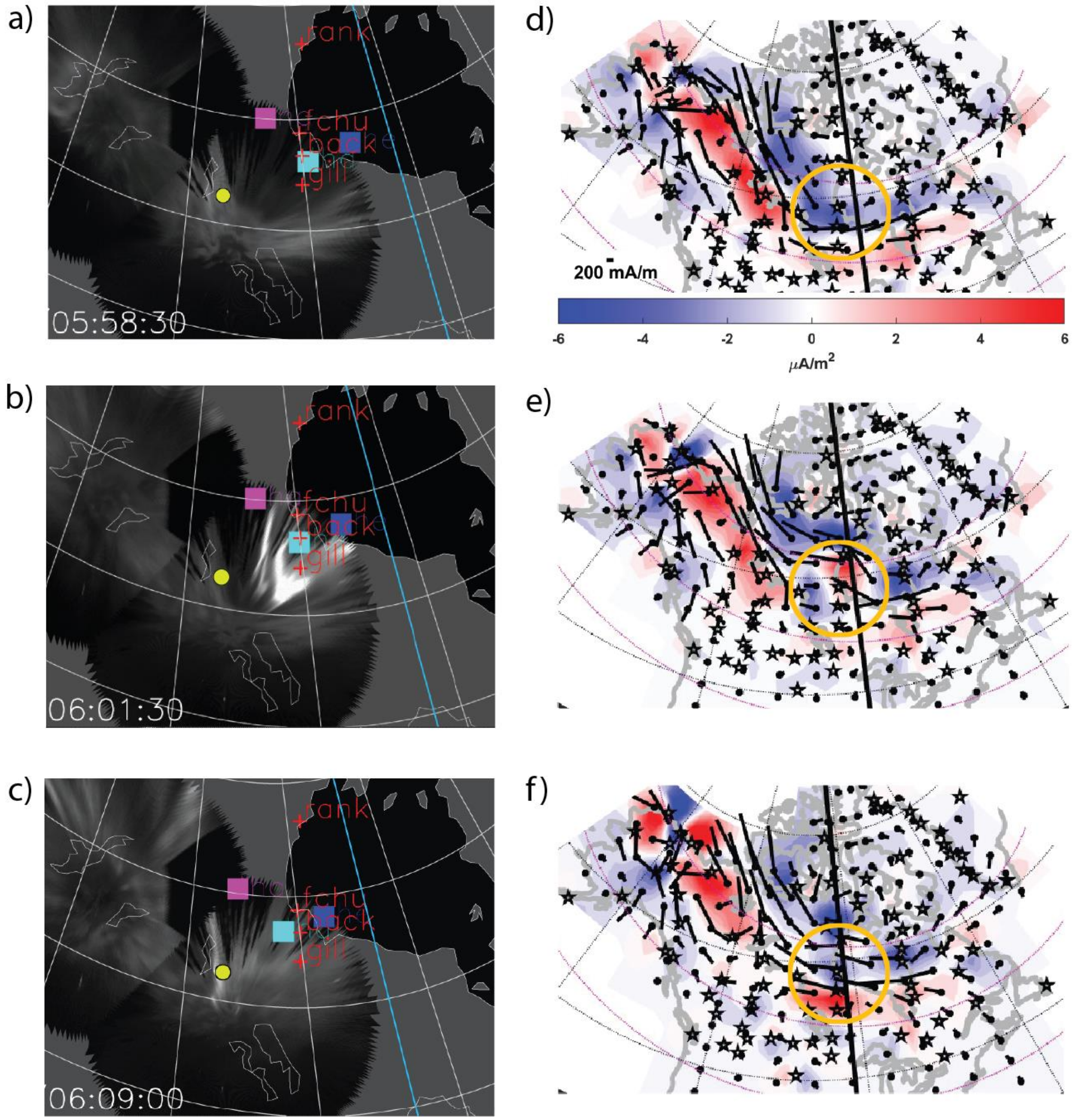

Figure 6. Composite all-sky auroral images and SECS maps as in Figure 5, but at 5:58:30, 6:02, and 6:09 UT on January 27, 2017.

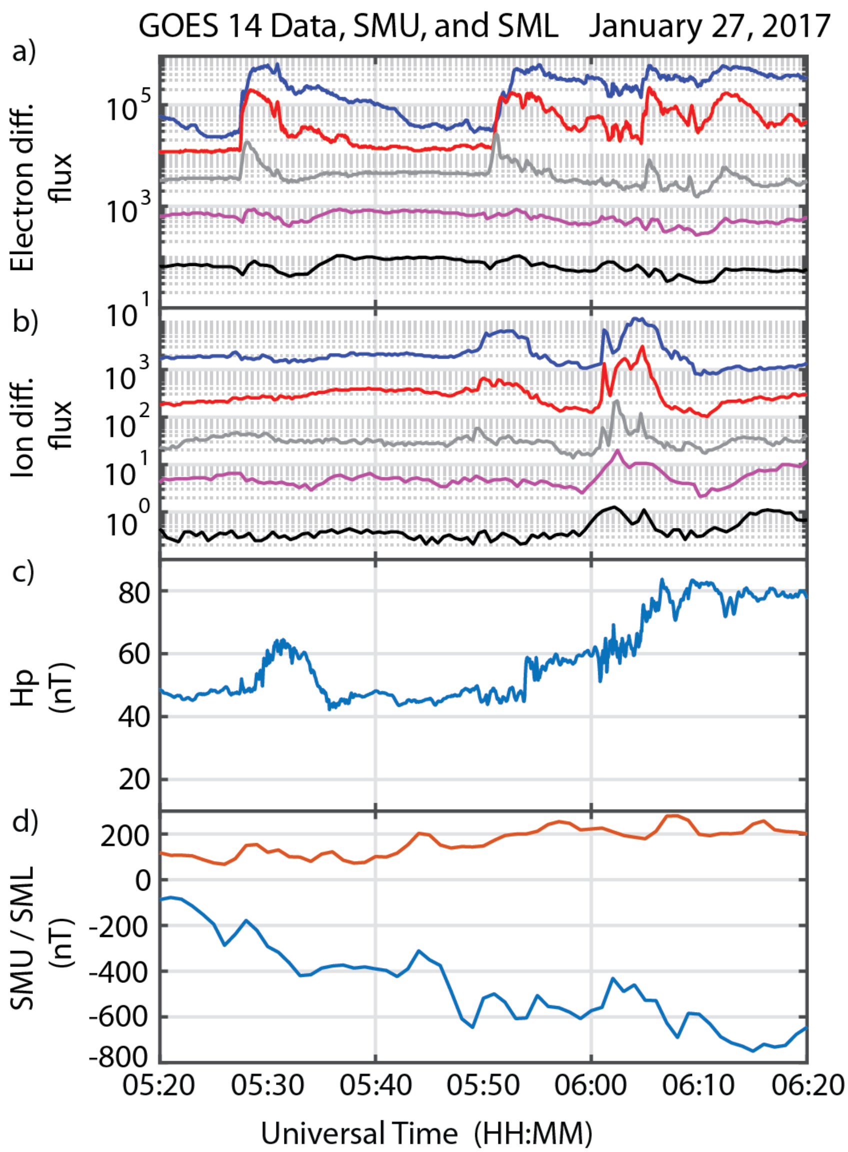

Figure 7. Stacked plots of GOES 14 energetic particle and magnetic field data and magnetic activity index data from 05:20 to 06:20 UT on January 27, 2017. Panel a shows the differential electron flux in five energy ranges (blue 30-50 keV, red 50-100 keV, grey 100-200 keV, pink 200-350 keV, and black 350-600 keV), and panel b shows ion flux in five energy ranges (blue 80-110 keV, red 110-170 keV, grey 170-250 keV, pink 250-350 keV, and black 350-800 keV), respectively, both in units of $cm^{-2} s^{-1} sr^{-1} keV^{-1}$. Panel c shows the Hp component (approximately northward) of the magnetic field from the outboard magnetometer. Panel d shows the SMU (red) and SML (blue) auroral activity indices.

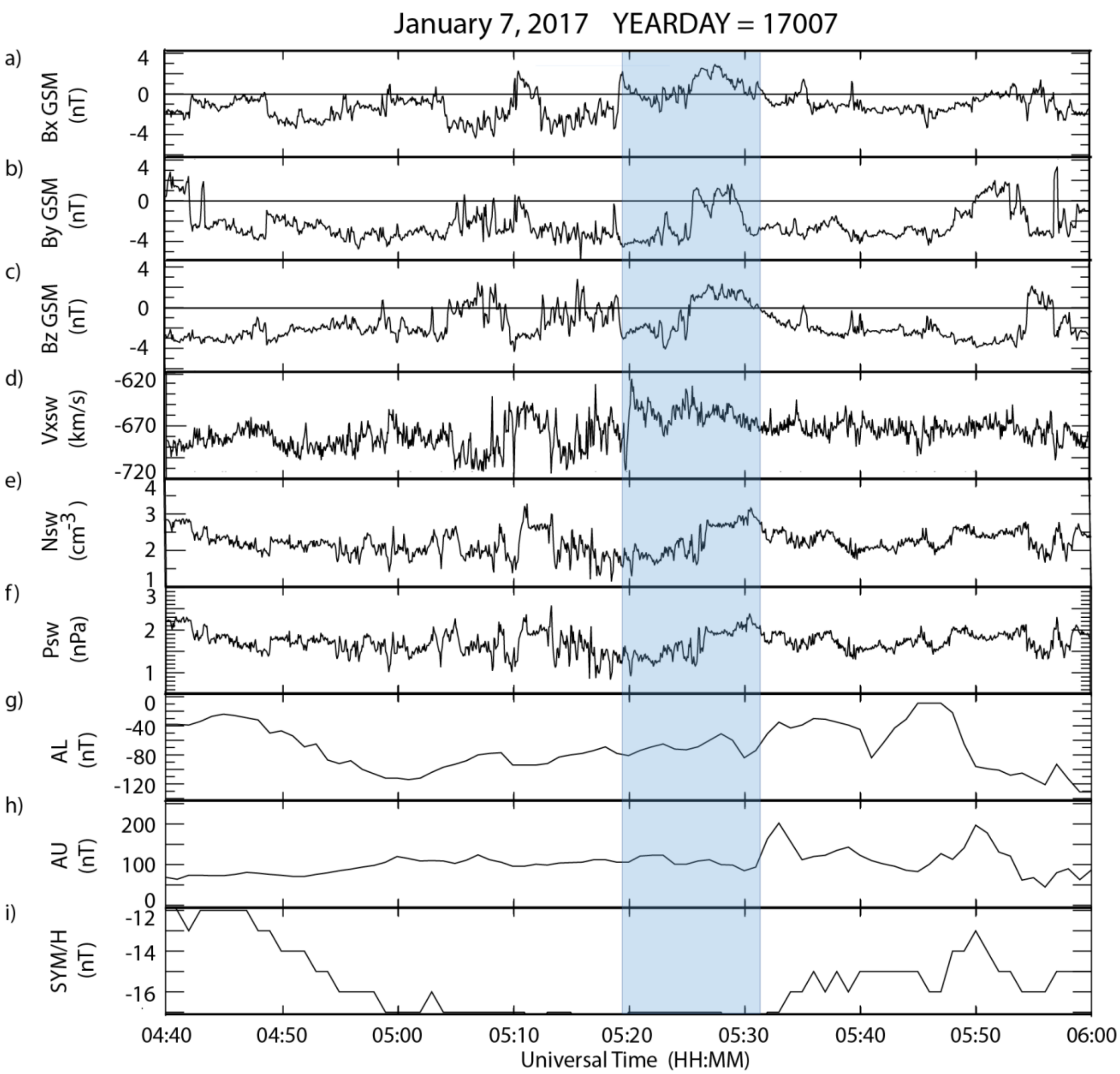

Figure 8. ARTEMIS P2 (THEMIS C) IMF and solar wind data time-shifted to the nose of the bow shock (panels a-f), and AL, AU, and SYM/H magnetic activity indices (panels g-i) from 04:40 to 06:00 UT January 7, 2017, as in Figure 2. The shaded interval shows a time interval with nearly simultaneous DFBs observed by THEMIS E and GMDs observed by ground stations near the east coast of Hudson Bay.

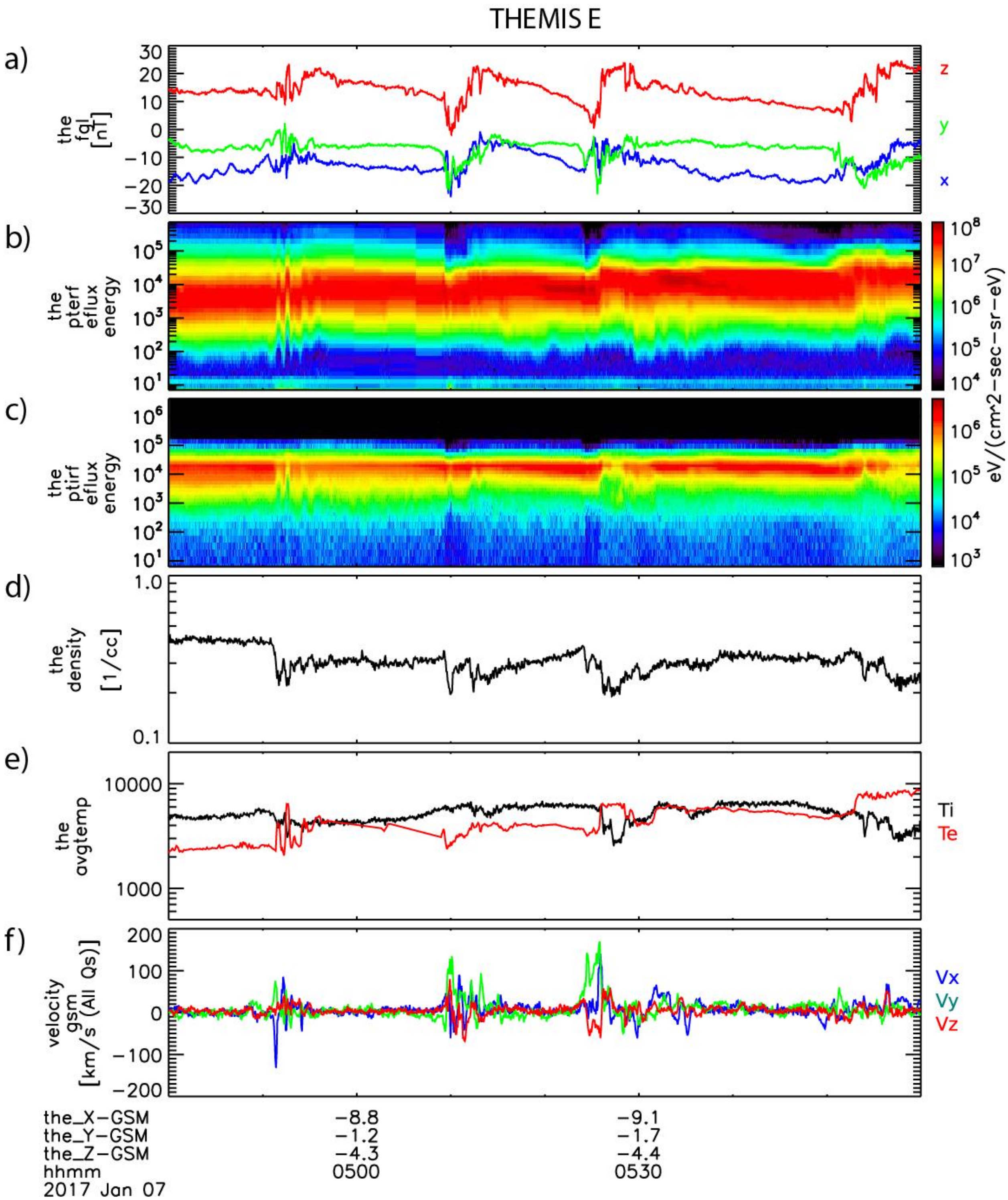

Figure 9. THEMIS E overview from 04:40 to 06:00 UT January 7, 2017, as in Figure 3.

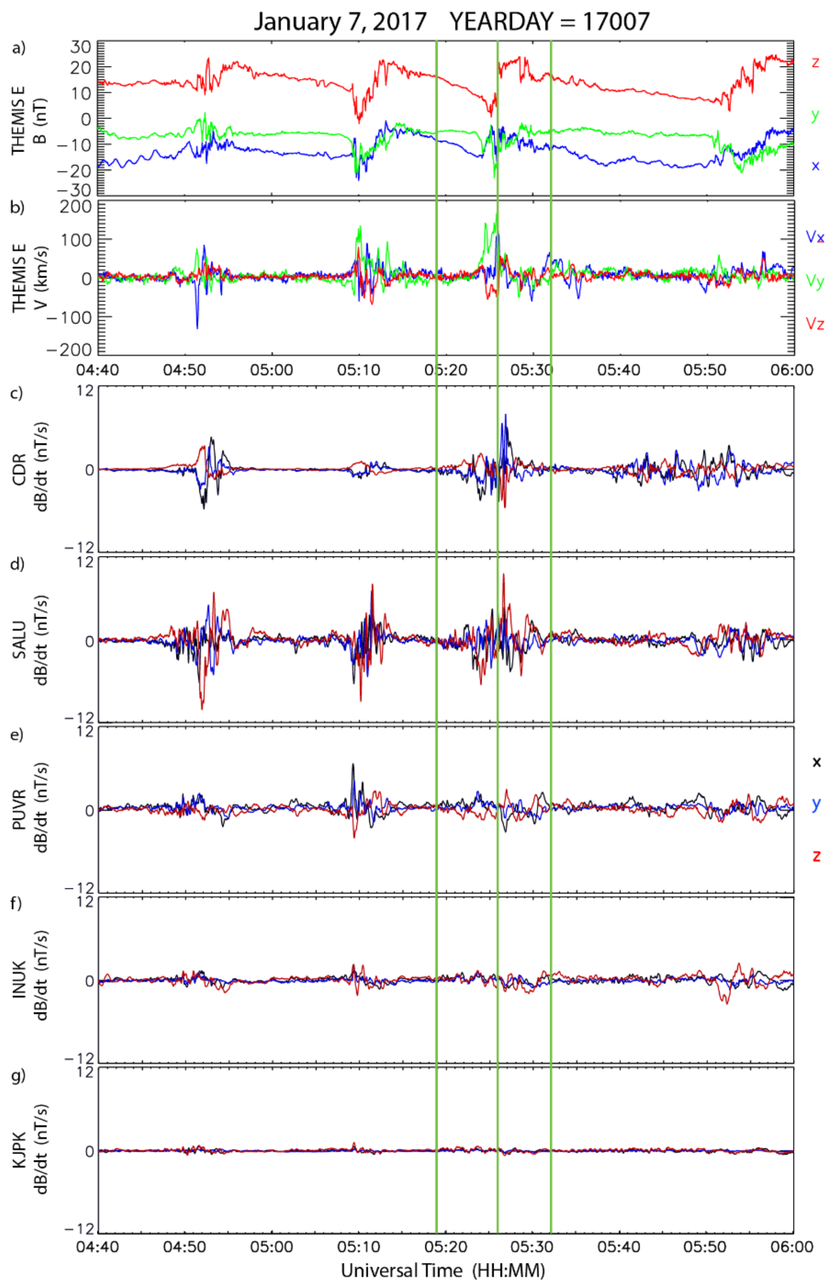

Figure 10. Composite plot showing simultaneous observations the magnetic field and bulk velocity observed by THEMIS E and the magnetic field observed by five ground-based magnetometers, in order of decreasing latitude, from 04:40 to 06:00 UT January 7, 2017, as in Figure 5. Panels c - g show three components of the time derivative of the magnetic field from Cape Dorset, Salluit, Puvirnituq, Inukjuak, and Kuujuarapik, respectively, in local geomagnetic coordinates. The vertical green lines correspond to the times of SECS maps and composite all-sky images shown in Figure 11.

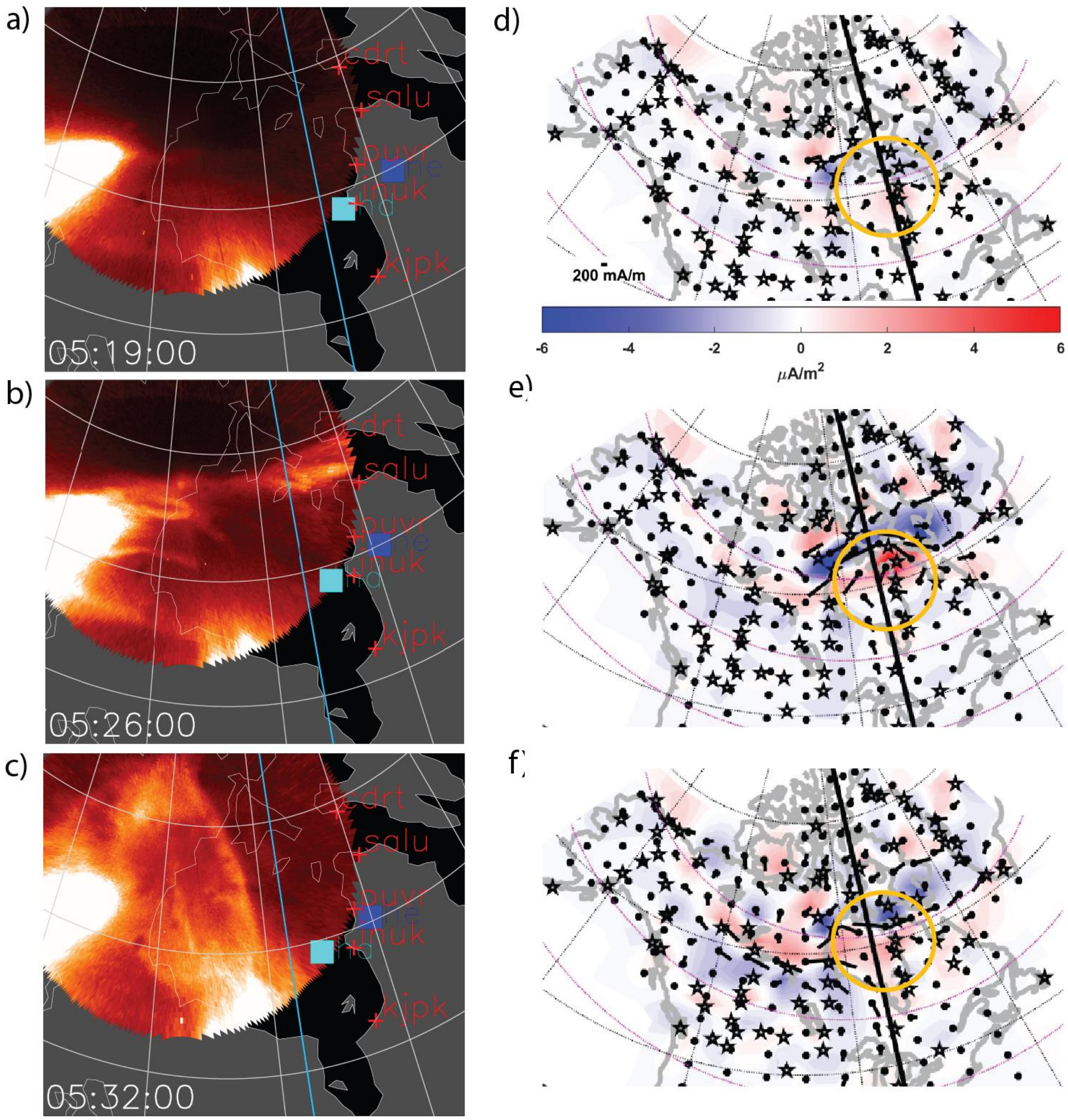

Figure 11. Composite all-sky auroral images and SECS maps as in Figure 5, but at 5:19, 5:26, and 5:32 UT on January 7, 2017.

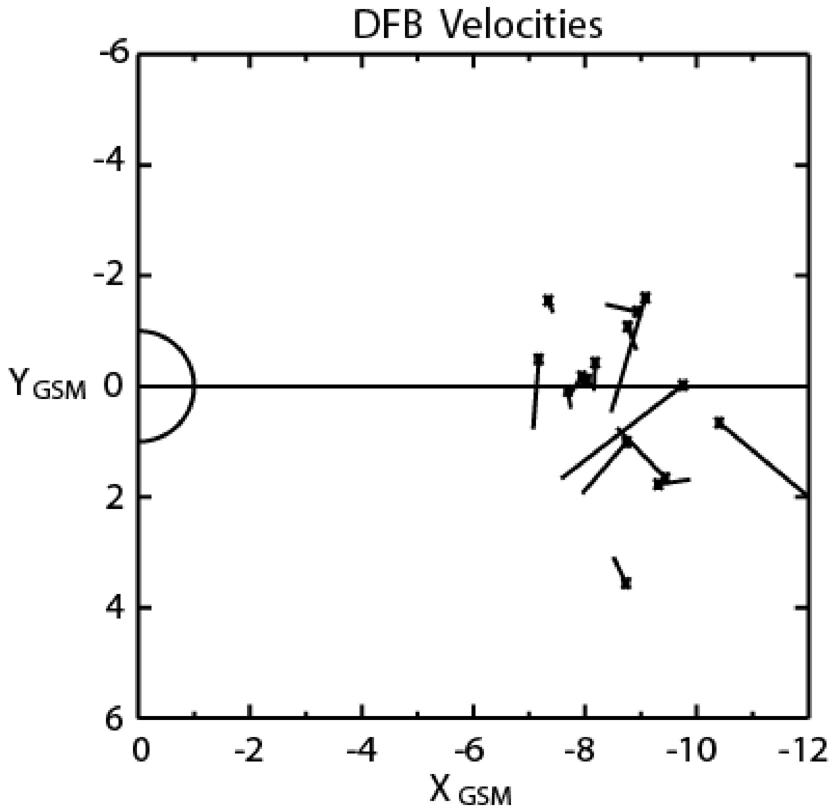

Figure 12. Plot of the locations and velocities of DFBs observed in the XY_{GSM} plane during near-simultaneous DFB – GMD events.

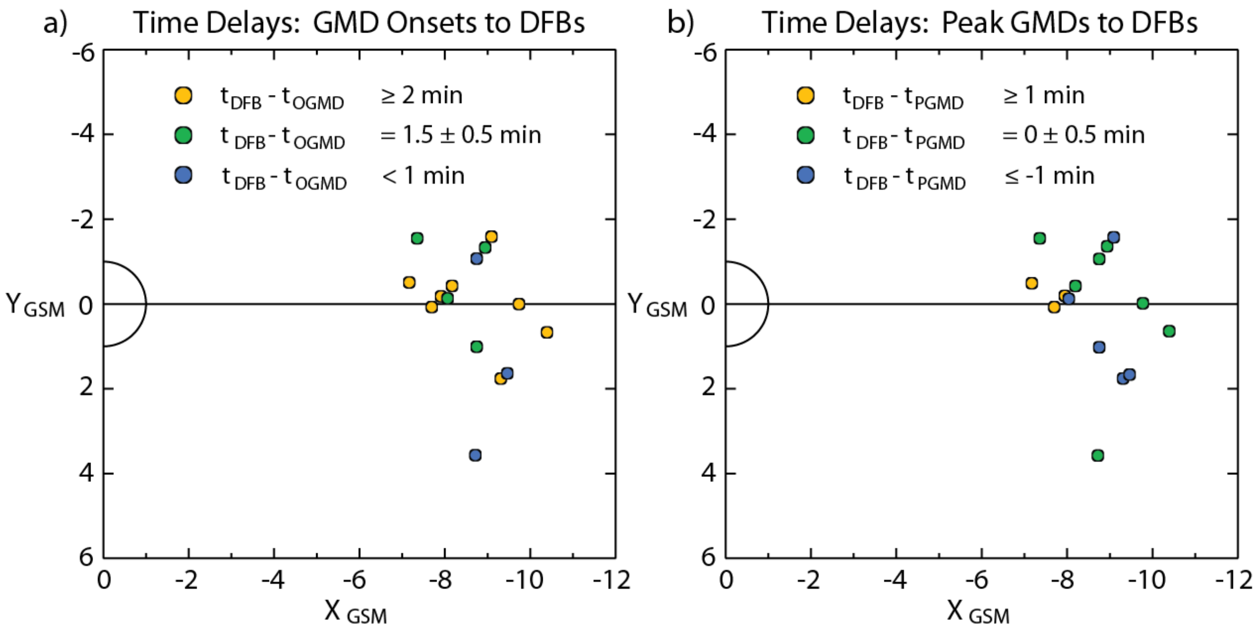

Figure 13. a) The time difference between the time of GMD onsets and DFBs, and b) The time difference between the time of the peak GMD derivatives and DFBs, respectively, for the events listed in Table 4.

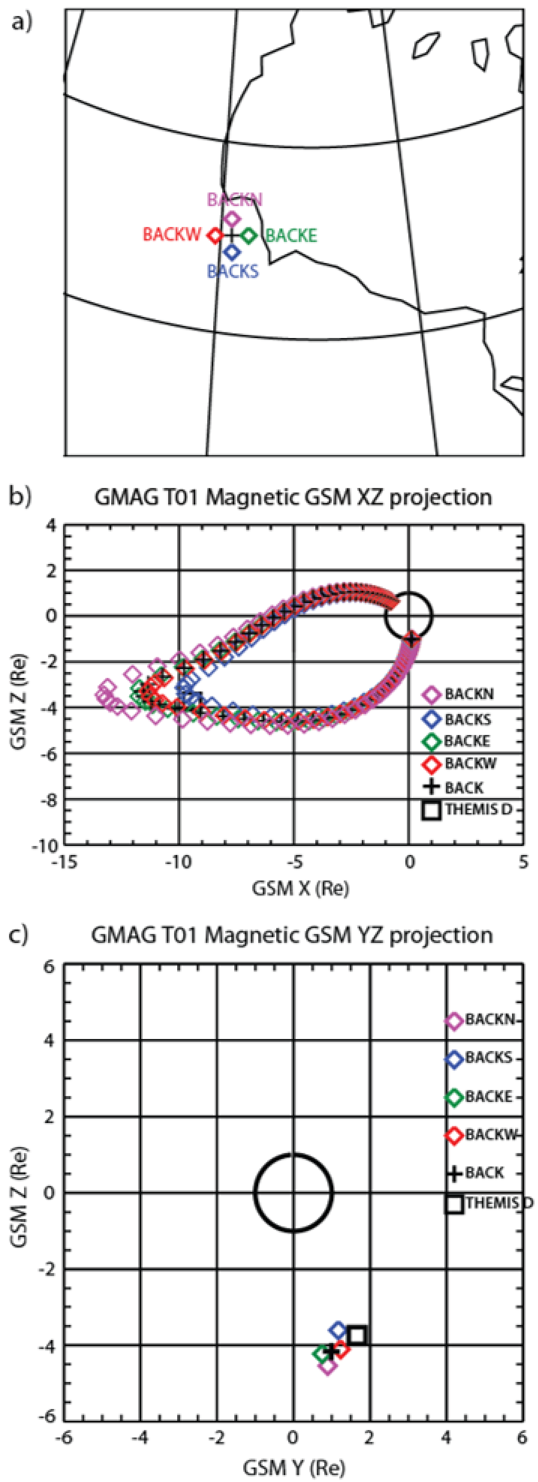

Figure 14. a) Map of the region near the southwest corner of Hudson Bay, Canada showing the location of BACK (cross) and locations 50 km north (BACKN), south (BACKS), west (BACKW) and east (BACKE) of BACK (colored diamonds). b) Traces of the mapped magnetic field lines from these five locations (cross and diamonds) in a GSM Z-X grid tailward from the northern ionosphere to the neutral sheet and earthward again toward the southern ionosphere. The GSM Z-X location of THEMIS D (black square) is also shown. c) Plots of the Z_{GSM} and Y_{GSM} locations of THEMIS D and these mapped field lines south of the neutral sheet at a tailward distance of $X_{GSM} = -9.43\ R_E$.

1201